Original Paper

New model of linkage evolution for the transtensional fault systems in the Nanpu Sag of Bohai Bay Basin: Insight from seismic interpretation and analogue modelling

Yu-Heng Wang [a], Fu-Sheng Yu [a, b, *], Bao-Yin Zhao [c], Ling-Jian Meng [c]

[a] College of Geosciences, China University of Petroleum (Beijing), Beijing, 102249, China
[b] State Key Laboratory of Petroleum Resources and Prospecting, China University of Petroleum (Beijing), Beijing, 102249, China
[c] Jidong Oilfield Company, PetroChina Limited Company, Tangshan, 063004, Hebei, China

A B S T R A C T

The evolution of faults within the same stress field is frequently influenced by numerous factors, involving the reactivation of pre-existing structures, stress transmission through ductile detachment layers, and the growth, interaction, as well as linkage of new fault segments. This study analyses a complex multi-phase oblique extension fault system in the Nanpu Sag (NPS) of the Bohai Bay Basin (BBB), China. High-resolution three-dimensional (3D) seismic data and analogue modelling indicate that the oblique extensional reactivation of pre-existing structures governs the sequential arrangement of fault segments in the caprock, and they dip synthetically to the reactivated fault at depth. During the NW−SE extension in the Eocene, the predominant movement of the pre-existing fault is strike-slip. Subsequently, during the N−S extension since the Oligocene, inclined at $20°$ to the pre-existing fault, forming splay fault segments and ultimately creating large en-échelon arcuate faults linked by relay ramps. Using fault throw-distance (T-D) and laser scanning, we reconstructed the fault evolution model of oblique extension reactivation in the presence of a ductile detachment basement. Our study illustrates that the arcuate faults can be categorized into linear master fault segments controlled by pre-existing structures, bending splay faults in the termination zone, and normal fault segments responding to the regional stress field. The interaction between faults occurs among normal faults and strike-slip faults, and the kinematic unification of the two fault systems is accomplished in the intersection zone. As the faults continue to evolve, the new fault segments tend to relinquish the control of pre-existing structures and concentrate more on the development of planar and continuous major faults. The ductile detachment layer significantly contributes to the uniform distribution of strain, resulting in narrow shear zones and discontinuous normal faults in its absence.

© 2024 The Authors. Publishing services by Elsevier B.V. on behalf of KeAi Communications Co. Ltd. This is an open access article under the CC BY-NC-ND license (http://creativecommons.org/licenses/by-nc-nd/4.0/).

1. Introduction

En-échelon faults frequently exhibit multiple interpretive models. Owing to their distinctive stepping pattern, they have been interpreted as either the oblique extension reactivation of pre-existing structures propagating upwards (Dunbar and Sawyer, 1989; Cloetingh et al., 1995; Henza et al., 2010; Duclaux et al., 2020; Deng and McClay, 2021), leading to the development of young en-échelon faults in the caprock (Fig. 1(a)). They are also interpreted as the releasing bends (Cunningham and Mann, 2007; Fodor, 2007; Dooley and Schreurs, 2012) and the accommodation of localized extension in the strike-slip fault termination zones (Fig. 1(b) and (c)). Within this termination zone, extension and strike-slip components are accommodated by en-échelon splay faults (Fig. 1(d)), referred to as "horsetail splay faults" or "extensional imbricated fan" structure (Woodcock and Fischer, 1986; Basile and Brun, 1999; Gabrielsen et al., 2001; Kim and Sanderson, 2006; Arfaoui et al., 2017). The main difference between the two theories lies in whether there is a linear principle displacement zone (PDZ). Over the past three decades, sustained research activity
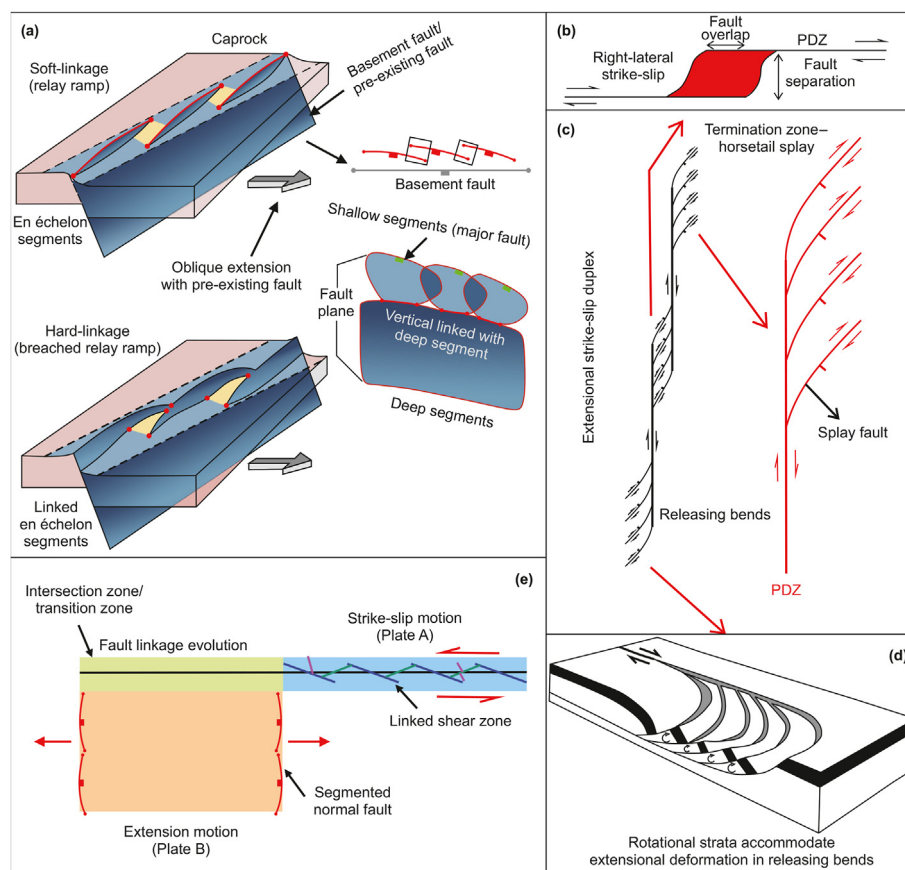
Fig. 1. Various genesis models of en-échelon faults. **(a)** Synoptic 3D models of oblique reactivation of a basement fault. En échelon fault segments form in the cover sequence above the basement fault. Overlapping, "soft-linked" by 3D relay ramps, breaching of the "soft linkages" into hard linkage (modified after Fossen and Rotevatn, 2016; Deng and McClay, 2021). **(b)** Pull-apart basin in the overlapping zone of the releasing bends (modified after Mann, 2007). **(c)** Extensional strike-slip duplex and its termination zone (modified after Woodcock and Fischer, 1986). **(d)** 3D model of lithospheric rotation accommodating extensional displacement (modified after Woodcock and Fischer, 1986). **(e)** Displacement transfer model for a two-plate intersection translation in this article (modified after Mouslopoulou et al., 2007).

has focused on normal fault growth through segment linkage or strike-slip fault growth through step-over (Fig. 1(a) and (e)). Some scholars have established models based on outcrop observations (Dunbar and Sawyer, 1989; Cartwright et al., 1995; Gawthorpe and Leeder, 2000; Wilson et al., 2009; Fossen and Rotevatn, 2016), analysed subsurface fault relationships through seismic data (Soliva and Benedicto, 2004; Morley et al., 2007; Deng and McClay, 2021), and reconstructed fault evolution processes through analogue modelling (Exadaktylos et al., 2003; Hus et al., 2005; Wyrick et al., 2011; Duclaux et al., 2020; Zwaan et al., 2020). Indeed, it involves interactions among various types of faults. No simulation experimental results proving this method have been presented yet. When a strike-slip fault intersects with a normal fault, the termination zone of the strike-slip fault undergoes bending, and the slip vector gradually steepens to accommodate the dip-slip component generated during the extension phase. In circumstances where faults are synchronously active, linkage evolution promotes displacement transfer and kinematic consistency within the fault system (Mouslopoulou et al., 2007).

In this study, we analyse a transtensional fault system in the NPS, which is part of the inboard rift system of eastern China and has undergone multi-phase extension in different directions (Fig. 2). Here, the pre-existing uplift in the Eocene controls the combination of fault reaction and later oblique extension, giving rise to a series of en-échelon splay faults. Our study has revealed: (1) The arcuate transtensional fault comprises moderately to normal fault segments, curved splay fault segments, and linear strike-slip fault segments. (2) The progressive bending of splay faults and the offset of relay ramps accommodate the non-coupling of displacement fields. (3) The interaction between different fault segments occurs at various stages through relay ramps, gradually enhancing the connectivity relationship until they eventually merge into a cohesive whole. (4) The uniform distribution of ductile detachment layers is crucial for the progressive evolution. Our study contributes to understanding the linkage evolution among different types of faults. The complex interconnection process among faults in this model also leads to the development of more relay ramps, which is beneficial for oil and gas exploration.

2. Geological setting

The BBB is situated in the intracontinental centre of the North China Craton (Fig. 2(a)), subjected to the intense convergence of surrounding tectonic plates (Liang et al., 2022). Interpretations of the Cenozoic BBB over the past three decades have included various models, such as the pull-apart model (Schellart and Lister, 2005; Tong et al., 2013), rift model caused by extension superimposed by strike-slip motion (Qi and Yang, 2010; Hu et al., 2022; Chen et al., 2022), and multi-phase rifting models in different directions (Allen et al., 1997; Li et al., 2012; Yu and Koyi, 2016; Zhu et al., 2021; Liang et al., 2022). The transition between extensional and compressive backgrounds results in significant angular unconformities throughout the basin, indicating truncation between the Cenozoic and Mesozoic (Fig. 3). Nowadays, it is well
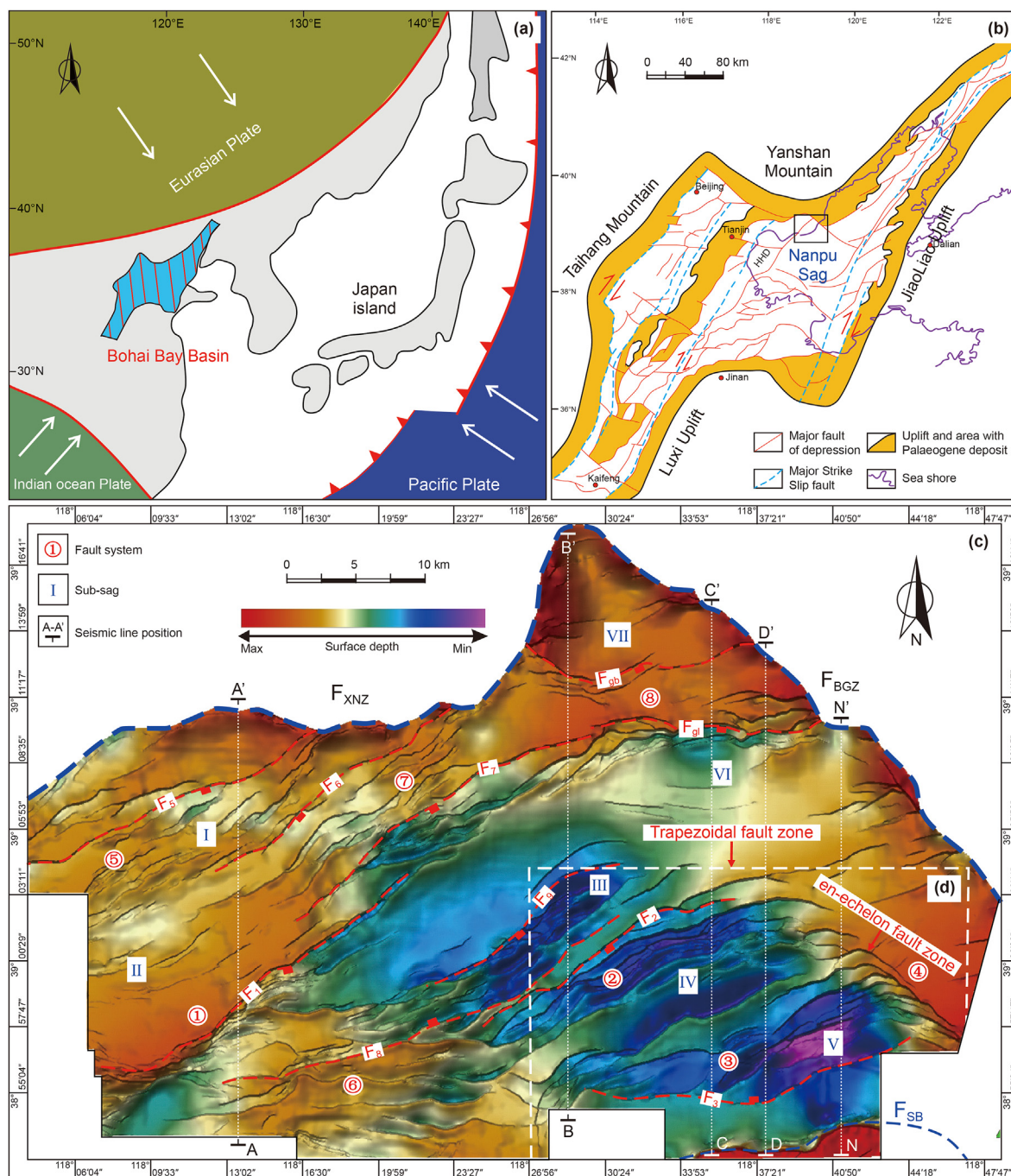
Fig. 2. Cenozoic structural map of the Nanpu Sag in the Bohai Bay Basin and its regions showing major elements. **(a)** Tectonic map of east Asia with the location of the Bohai Bay Basin. **(b)** Tectonic units of Bohai Bay Basin (modified after Yu and Koyi, 2016). **(c)** Structural units of Nanpu Sag. **(d)** Location of study area. I: Xinanzhuang sub-sag; II: Beipu sub-sag; III: Linque sub-sag; IV: North sub-sag of Caofeidian; V: South sub-sag of Caofeidian; VI: Liunan sub-sag; VII: Shichang sub-sag; ①: FZ①; ②: FZ②; ③: FZ③; ④: FZ④; ⑤: FZ⑤; ⑥: FZ⑥; ⑦: Miaonan Fault zone; and ⑧: Gaoliu-Gaobei Fault zone. Unique fault names in Nanpu Sag: F_{XNZ}, F_{BGZ}, F_{SB}, F_{gl}, and F_{gb}.

acknowledged that the basin has mainly experienced two tectonic events in the Cenozoic: the Paleogene sys-rift period and the Neogene post-rift period (Allen et al., 1997; Li et al., 2012; Yu and Koyi, 2016; Xu et al., 2018; Zhu et al., 2021). Deposition in the Eocene was mainly controlled by NE-trending syn-rift faults, resulting in isolated half-graben structures. The basin was dominantly influenced by EW-trending syn-rift faults in the Oligocene, gradually evolving into complete graben structures and forming a unified deposition centre after the Miocene. Therefore, the widely accepted hypothesis suggests a NW–SE rift during the Eocene,

transitioning to a N–S rift after the Miocene (Allen et al., 1997; Qi and Yang, 2010; Li et al., 2012; Yu and Koyi, 2016; Xu et al., 2018; Zhu et al., 2021; Hu et al., 2022; Chen et al., 2022). During the period of changes in the rift direction, there were brief sedimentary interruptions, leading to the identification of angular unconformity interfaces in some localized areas. There was a truncation relationship between the Miocene and Eocene (Fig. 3). Despite the longstanding debates over the dynamic changes in the Cenozoic rift direction in the BBB, some scholars attribute its formation to regional extension induced by the subduction of the Western
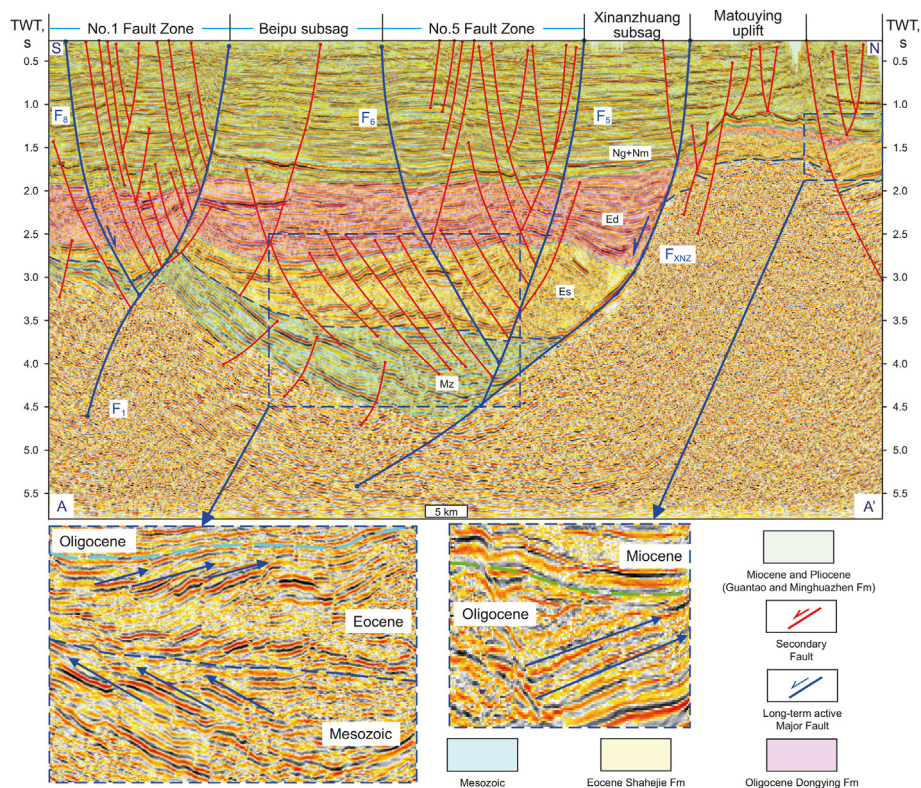
Fig. 3. Seismic section of unconformity in Nanpu Sag (for the locations of the sections, see Fig. 2(c)). The blue annotation represents the three crucial unconformities: bottoms of the Eocene, Oligocene, and Miocene. The onlap and truncation of the upper and lower strata, respectively, characterise the bottom of the Eocene unconformity. The weak onlap of the upper strata and evident truncation of the lower strata characterises the bottom of the Oligocene unconformity. Distinct truncation of lower strata characterises the bottom of the Miocene unconformity.

Pacific Plate, with adjustments in extensional direction following the cessation of plate subduction in the Miocene (Schellart and Lister, 2005; Liang et al., 2014; Yu and Koyi, 2016; Liang et al., 2022). Others propose an explanation based on the collision of the Indian Plate since the late Cenozoic (55 ± 10 Ma), resulting in localized mantle upwelling due to eastward dispersion in the deep mantle (Liu et al., 2004; Li et al., 2012; Zhao et al., 2019).

The NPS is a typical half-graben lacustrine rift basin located in the northern part of BBB. Sedimentation in the strata is primarily controlled by northern subsidence, gradually overlaying towards the south (Liu and Zhang, 2011; Tong et al., 2013; Liang et al., 2014; Zhao et al., 2019). It is surrounded by the Yanshan Mountains to the north, the Shaleitian Uplift to the south, directly interconnected to the Qikou Depression in the east and Bozhong Depression in the west (Fig. 2(b)). It is characterised by a distinct structural pattern, which includes a NE-trending fault system comprising faults F_1, F_2, F_3, F_5, F_6, F_7, and F_8, and an EW-trending fault system comprising faults F_{gl} and F_{gb}. A NW-trending en-échelon fault zone is observed in the southeastern part of the sag (Fig. 2(c)). The presence of these intersecting faults resulted in the sag being divided into seven distinct sub-sags (Fig. 2(c)), including the Xinanzhuang sub-sag, Beipu sub-sag, Linque sub-sag, north sub-sag of Caofeidian, south sub-sag of Caofeidian, Shichang sub-sag, and eight Fault zones (No. 1, No. 2, No. 3, No. 4, No. 5, No. 6, Miaonan, and Gaoliu—Gaobei Fault zone).

Based on our interpretation of well and seismic data, the interior of NPS predominantly consists of Cenozoic strata. In localized areas, remnants of sedimentation from the Paleozoic and Mesozoic periods were preserved. From the bottom to top, it contains five Formations (Fm) in different periods: the Eocene Shahejie Fm (Es),

Oligocene Dongying Fm (Ed), Miocene Guantao Fm (Ng), Pliocene Minghuazhen Fm (Nm), and overlying Quaternary strata (Fig. 4). The Es is divided into three members (Mbr), of which the third Mbr of the Shahejie Fm (Es_3) has relatively thick sedimentary strata (600—2000 m) comprising thick mudstone and a small amount of sandstone (Liu and Zhang, 2011; Tong et al., 2013; Liang et al., 2014; Zhao et al., 2019). The thick mudstone formed extensively distributed detachment zones within the study area. The Ed comprises three Mbrs, with thicknesses ranging from 650 to 1000 m, 300—550 m, and 400—800 m in ascending order (Fig. 4). The sedimentary deposits of the Miocene, with a thickness ranging from 800 to 1400 m, are extensively distributed within the basin (Fig. 4). The Pliocene is characterised by the significant thickness of sedimentary deposits ranging from 1100 to 1900 m, with mudstone at the bottom and interbedded sand-mudstone in the middle and upper parts (Liu and Zhang, 2011; Tong et al., 2013; Zhao et al., 2019). Additionally, white massive conglomerates exist at the bases of the Oligocene and Miocene, marking the occurrence of tectonic events between the Cenozoic sedimentary sequences. In the seismic profile, it is evident that these two interfaces exhibit a clear truncation relationship (Fig. 3).

3. Data and methods

3.1. Data

This study was primarily based on interpreting 3D seismic data that constrain major faults and seismic horizons in the Cenozoic. The seismic data were obtained from two surveys. One survey provided the seismic data (acquired in 2014) of the entire NPS with
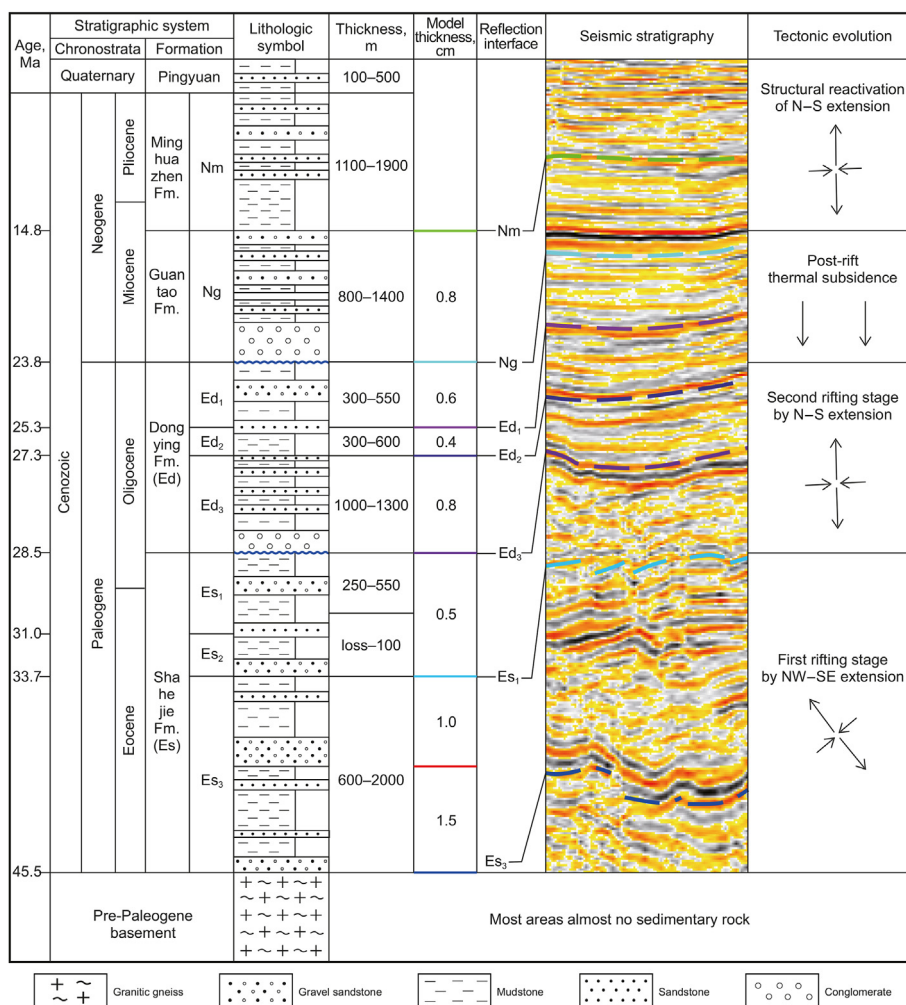
Fig. 4. Chart showing the stratigraphic column and tectonic evolution in NPS. Names of critical stratigraphic and seismic reflection layers are provided, and a seismic reflection section illustrates the typical seismic horizons in the area. Horizons that correlated with the seismic data through synthetic seismograms were mapped regionally. Each horizon code represents the bottom of the stratigraphic zone.

a lower dominant frequency (24—35 Hz) (Fig. 2(c)). This survey has an inline (N—S) and crossline (E—W) spacing of 25 m × 25 m, 1 ms vertical sample rate, covers an area of ~1900 km² and has a record length of ~45 km. There are 2888 inlines and 2511 crosslines in the data volume. It accounted for the geometry of the fault zone and transformation of the extension direction in each period. The other survey provided the local data volume of Fault zone No. 4 (FZ④), which was acquired in 2020 (Fig. 5(b)) and has a higher dominant frequency (33—42 Hz). This survey has an inline (NE—SW) and crossline (NW—SE) spacing of 12.5 m × 12.5 m, 1 ms vertical sample rate, covers an area of ~240 km² and has a record length of ~12 km. There are 1537 inlines and 973 crosslines. To analyse the fault linkage evolution and transformation process of the strike-slip components for different periods in the FZ④, we interpreted seismic data and conducted fault throw analysis along the vertical fault direction in the primary fault area of the FZ④.

3.2. Methodology

Synthetic seismic seismograms were conducted in the NPS based on well and seismic data, using the Landmark software (Version: R5000.01) for seismic horizon tracking. The entire area is equipped with 93 exploration wells, evenly distributed throughout

the NPS. Details regarding the depth relationships and drilling locations can be found in Fig. A-1. The tectonic event was identified by marking the termination relationship of seismic reflection unconformities (Fig. 3). The interpreted seismic horizon was named consistently with the stratigraphic sequence (Fig. 4). Fault interpretation was performed using Geoframe software (Version: 4.5), and we identified 20 major faults (F_2, F_3, and f_1—f_{18}) as the boundary or interior major faults of the transtensional fault systems of the Nm (Fig. 5). The geometry of the fault zone was analysed according to the N—S direction seismic sections (Fig. 6). Major characteristics of transtensional faults were interpreted and analysed through nine seismic sections (Fig. 7). Based on the analysis of key unconformities, geometric characteristics, and extension directions, a structural evolution model was established using the Move software (Version: 2018, Fig. 8). Sandbox analogue modelling was conducted by setting up an equal proportion of strata sand layers (Fig. 9). The extension direction was same as that of the proposed evolution model. We maintained the sandbox analogue modelling stage to verify the evolutionary model. The detailed experimental parameters are indicated in Tables 1 and 2. The deformation process of the sandbox experiment was analysed through interpretation of the top surface and section photos of the deformation results (Figs. 10—13). Laser scanning of the sandbox's
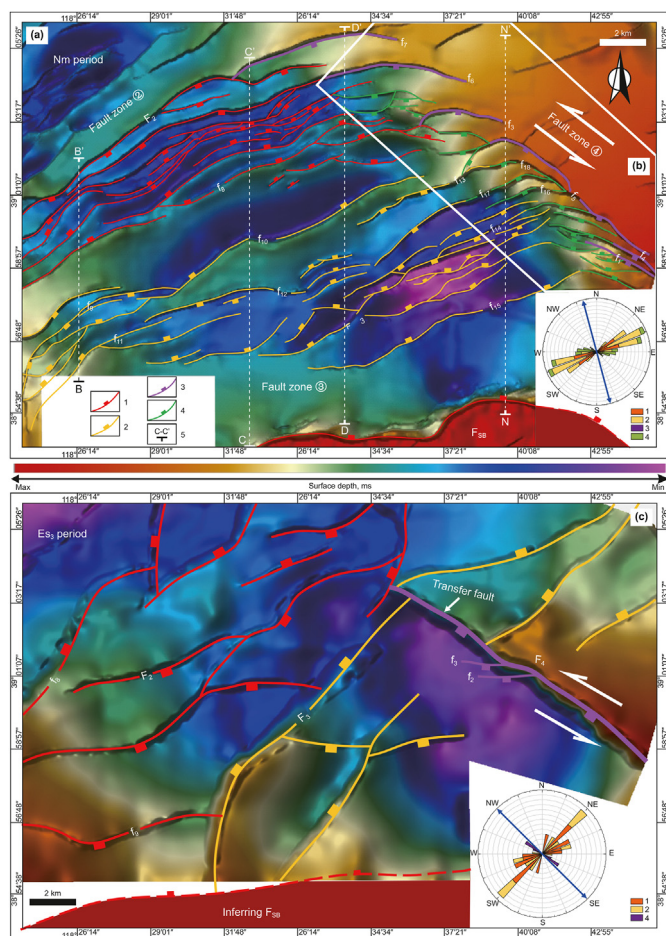
Fig. 5. 3D structural morphologies of trapezoidal fault zone at different periods. **(a)** Time-structure map for the Nm period. The main subsidence areas are located at FZ② and FZ③, while the FZ④ faults exhibit a predominant en-échelon arrangement. The main fault trend is oriented in a NWW direction. **(b)** Location of survey 2 (white rectangle). **(c)** Time-structure map for the Es$_3$ period. The location of the Fault F$_{SB}$ is inferred based on (Liang et al., 2014) estimation. The FZ④ region exhibits a distinct south-high and north-low morphology. 1: Faults F$_2$, f$_8$ in the FZ②; 2: Faults F$_3$, f$_9$, f$_{10}$, f$_{11}$, f$_{12}$, f$_{13}$, f$_{14}$, and f$_{15}$ in the FZ③; 3: Major strike-slip faults f$_1$, f$_2$, f$_3$, f$_4$, f$_5$, f$_6$, and f$_7$ in FZ④; 4: Splay faults and 5: location of the seismic section.

top surface (Scan Studio software, Version: Ultra) was employed for modelling (Fig. 14) and reconstructing its specific elevation shape through Petrel software (Version: 2018). The established evolution model was verified by comparing the experimental results with nature (Fig. 15). Furthermore, based on horizons and faults interpreted via seismic data and analogue modelling, statistics of the fault throw were compiled in every section (Appendix B: Supplementary Tables 1–3). The surrounding correlation of each grid was calculated using a 2 × 2 grid setting. Three periods of coherent attribute extraction were conducted via Petrel software using the limit of interpretation horizon. Three periods (Es$_3$, Ed$_1$, and Nm) of the transtensional fault system were identified, and the throw of the transtensional fault system was calculated in the seismic section based on seismic interpretation results. Origin software was used to compile the T-D curve (Figs. 16 and 17). Finally, a progressive model related to oblique extension of pre-existing structures is ultimately summarized and proposed (Fig. 18).

4. Framework of the trapezoidal fault zone

The trapezoidal fault zone in the NPS represents a distinct fault

system displaying a relatively independent behaviour. The subdivision was based on the geometric features of the faults, such as their strike, dip angle, and interaction with secondary faults. Fig. 5 depicted 3D structural maps during the Nm and Es$_3$, respectively. The fault zone was subdivided into Fault zone No. 2 (FZ②) and Fault zone No. 3 (FZ③) dominated by extensional deformation, and FZ④ dominated by transtensional deformation (Figs. 2(c) and 5). The rose chart confirmed the change in the direction of regional extension, with a small amount of NE-trending faults during Es$_3$ and a concentration in the NEE direction during the Nm. The fault strikes of FZ② and FZ③ were mainly NEE, whereas that of FZ④ was NW (Fig. 5(a)). The geometry of the area was a combination of a horst between the north and south grabens, with the east side bounded by the overlapping échelon of FZ④ (Fig. 5(a)). The faults F$_{XNZ}$ and F$_{BGZ}$ penetrated all strata as listric faults (Fig. 6). The interior of the fault zone was subdivided into independent horst-graben combinations by the following faults: F$_2$, F$_3$, F$_7$–F$_9$, F$_{gl}$, F$_{gb}$, and f$_8$-f$_{13}$. The plan positions of these faults are shown in Fig. 5(a).

4.1. Normal fault system

The FZ② is identified as a graben combination in N*m*, which is bounded by faults F$_2$ and f$_8$ on the north and south sides, respectively (Fig. 5(a)). The structure extends for nearly 20 km in length and 4 km in width, with numerous secondary parallel faults in the NEE direction. The secondary fault is essentially planar with rare occurrences of en-échelon arrangement. The stepped graben is bounded by closely dipping secondary faults, creating a typical extensional structure. At the northeast end, it connects with the FZ④ to comprise the divergent end of a horsetail structure. This region exhibits very few faults in the Es$_3$, forming a horst structure. With the fault growth, fault strike was predominantly changed from 45° to 60°. In the Nm, the fault strike has been shifted to a more adjustive N−S extension direction.

Based on seismic interpretation, faults within the study area comprised both long-term active basement faults and newly generated faults in the later stage, which are marked separately in Fig. 6. The syn-rift sequence in Es, verified activity of the major fault, which served as pre-existing faults for the deformation of the later stage. The newly generated faults from the Oligocene to Pliocene were formed based on pre-existing faults (Fig. 6(a) and (b)). The FZ② featured conjugate normal faults in the shallow layers, with dip angles at 55°−70°, and the primary and secondary faults incline towards each other to form a graben in the upper layers. With the fault growth, deep faults from the Palaeozoic to the Eocene formed narrow horsts, displaying an "X" shaped structural style comprising several parallel faults (Fig. 6(a)). The large subsidence along the primary fault in Eocene, indicated a higher deformation intensity during the Eocene period. Contrastingly, the weaker subsidence controlled by shallow faults indicated weakening of fault activity at a later stage (Fig. 6(a) and (b)).

The FZ③ is termed as the graben in Nm, bounded by faults f$_9$, f$_{10}$, F$_3$, and f$_{11}$. The structure is approximately 24.5 km long and 6.7 km wide. On the northern side, faults f$_9$ and f$_{10}$ exhibit a small degree of overlap along their strike directions, with opposite dips. Fault f$_{10}$ controls a half-graben with a deepening towards the fault plane. Its footwall is in a relatively elevated position within the FZ③. The southern boundary faults F$_3$ and f$_{11}$ have the same strike but are discontinuous in the form of an en-échelon combination (Fig. 5(a)). The structure is characterised by a narrow graben combination in the southwest and a more comprehensive, gentle listric fault combination in the northeast. In the plan view, the structure connects with the FZ④ towards the northeast. The faults exhibit bending behaviour at the intersection of two structures and gradually turn towards the NEE direction. This zone had only seven
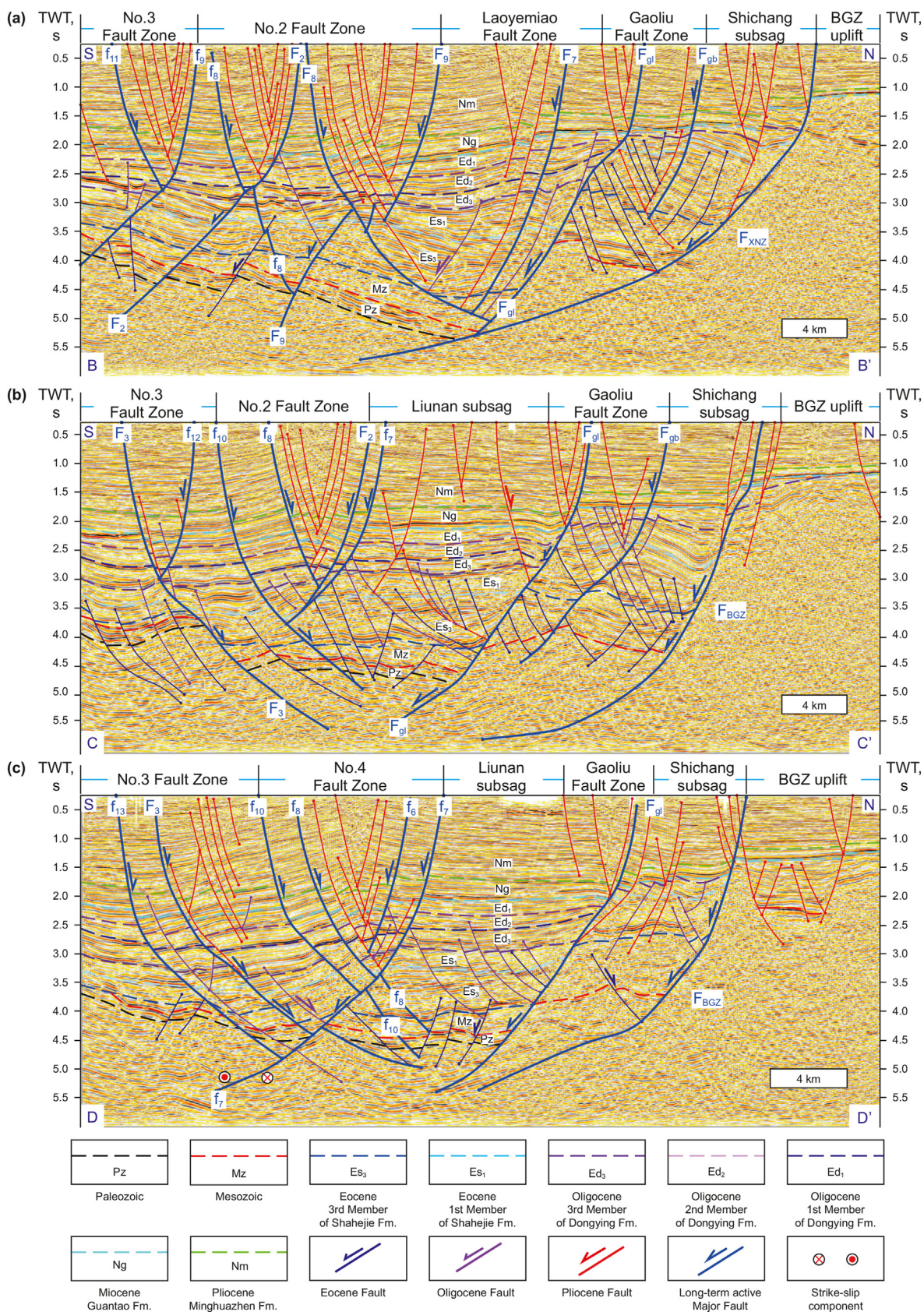
Fig. 6. Seismic section snippets showing the N–S cross-sections through the structures displaying the central units and their deformations (for the locations of the sections, see Fig. 2(c)). Sections from top to bottom are B–B', C–C', and D-D'. The arrows mark the strata rotation and sedimentation thickening owing to listric faults.
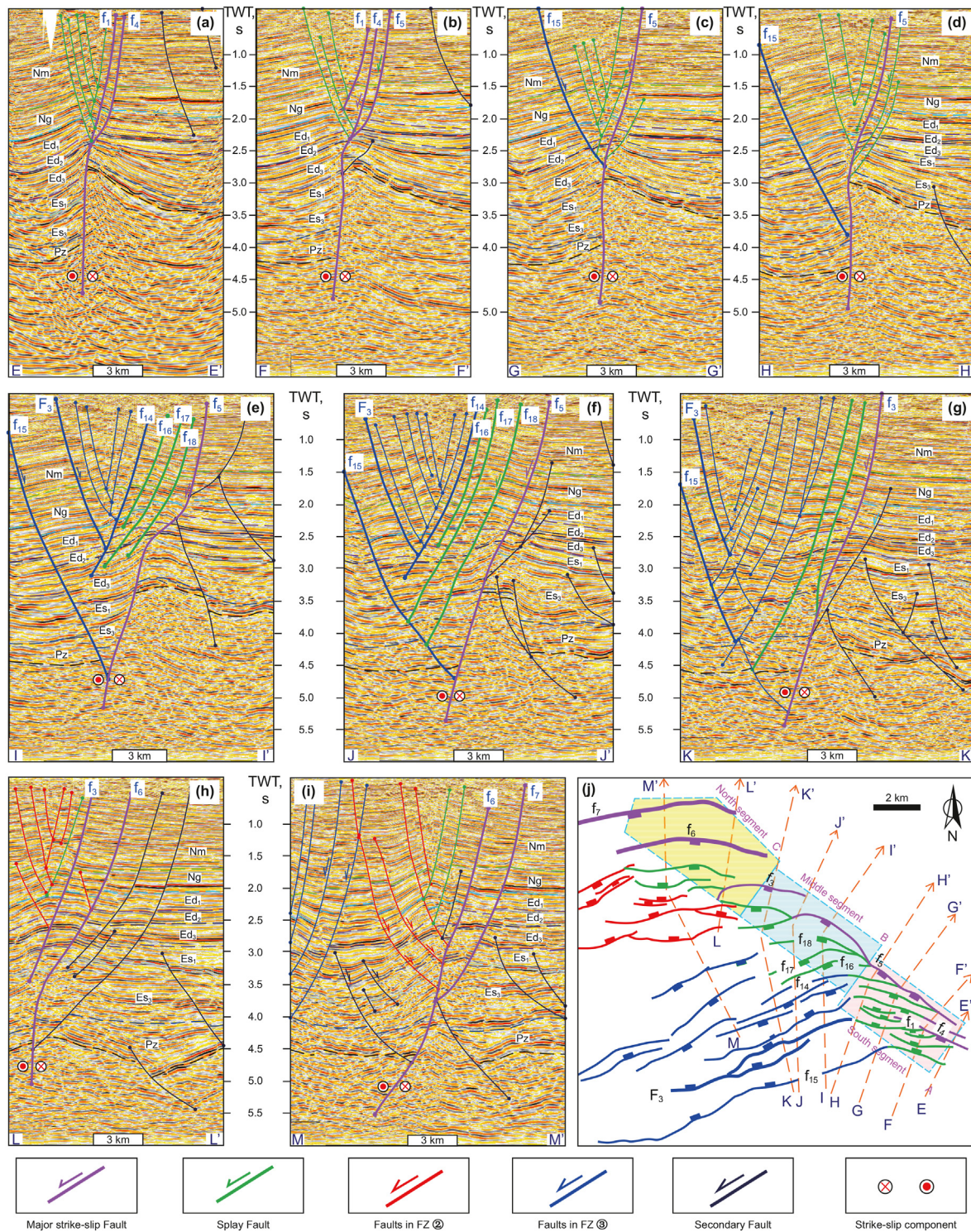
Fig. 7. Seismic sections illustrating the deformation characteristics of the transtensional fault system (for the legend of strata, see Fig. 6.). According to the geometric characteristics of the faults, the FZ④ is classified into three segments. The shallow fault segment linked with basement fault in southern segment has a nearly vertical dip angle, while the dip angle of the northern segment gradually decreases (for the locations of the sections, see Fig. 7(j)). The flower structures are primarily shown in Fig. 7(a)–(d).

isolated N-dipping normal faults, each controlling one half-graben. As the faults continued to grow, the isolated major faults evolved into en-échelon combination (Fig. 5(c)).

Seismic interpretation revealed that conjugate normal faults primarily characterise the FZ③, exhibiting dip angles ranging from 50° to 65°. The rotation of blocks and the development of a domino-style structural configuration result from the interaction of these three faults (F₃, F₁₃ and f₁₀). Fig. 7(e)–(g) depicts numerous secondary faults developed in the FZ③, although they were confined to the shallow layers and did not overlap with long-term active faults. The presence of this collapsed structure (McClay, 1990) indicates a background of rapid extension during the later
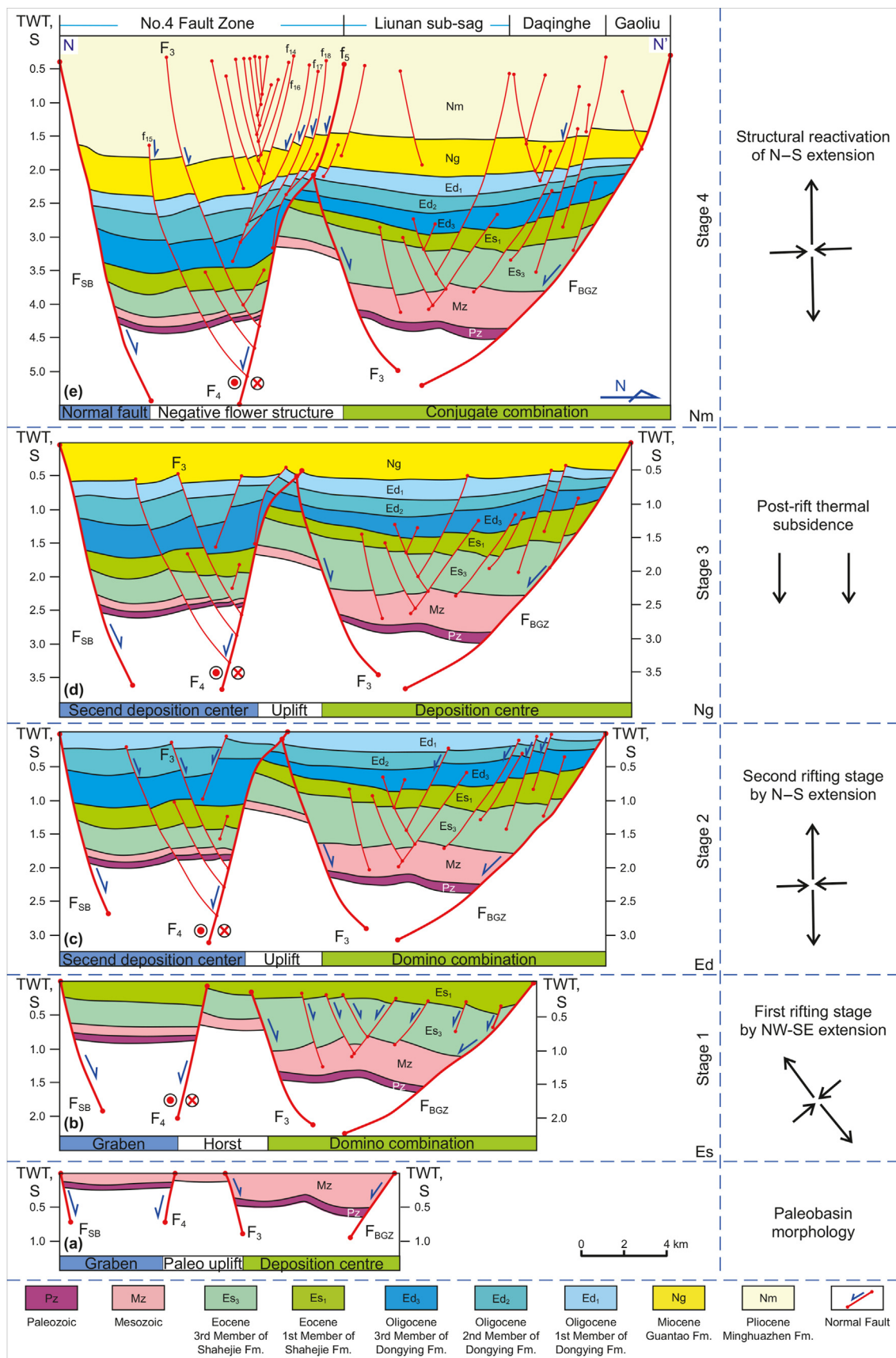
Fig. 8. Sequential schematic displaying the evolution of the trapezoidal fault zone from the Paleozoic to the present. The arrow indicates the extension direction applied to the region (for the locations of the sections, see Fig. 2(c)). Nm: Pliocene Minghuazhen Fm; Ng: Miocene Guantao Fm; Ed: Oligocene Dongying Fm; and Es: Eocene Shahejie Fm.
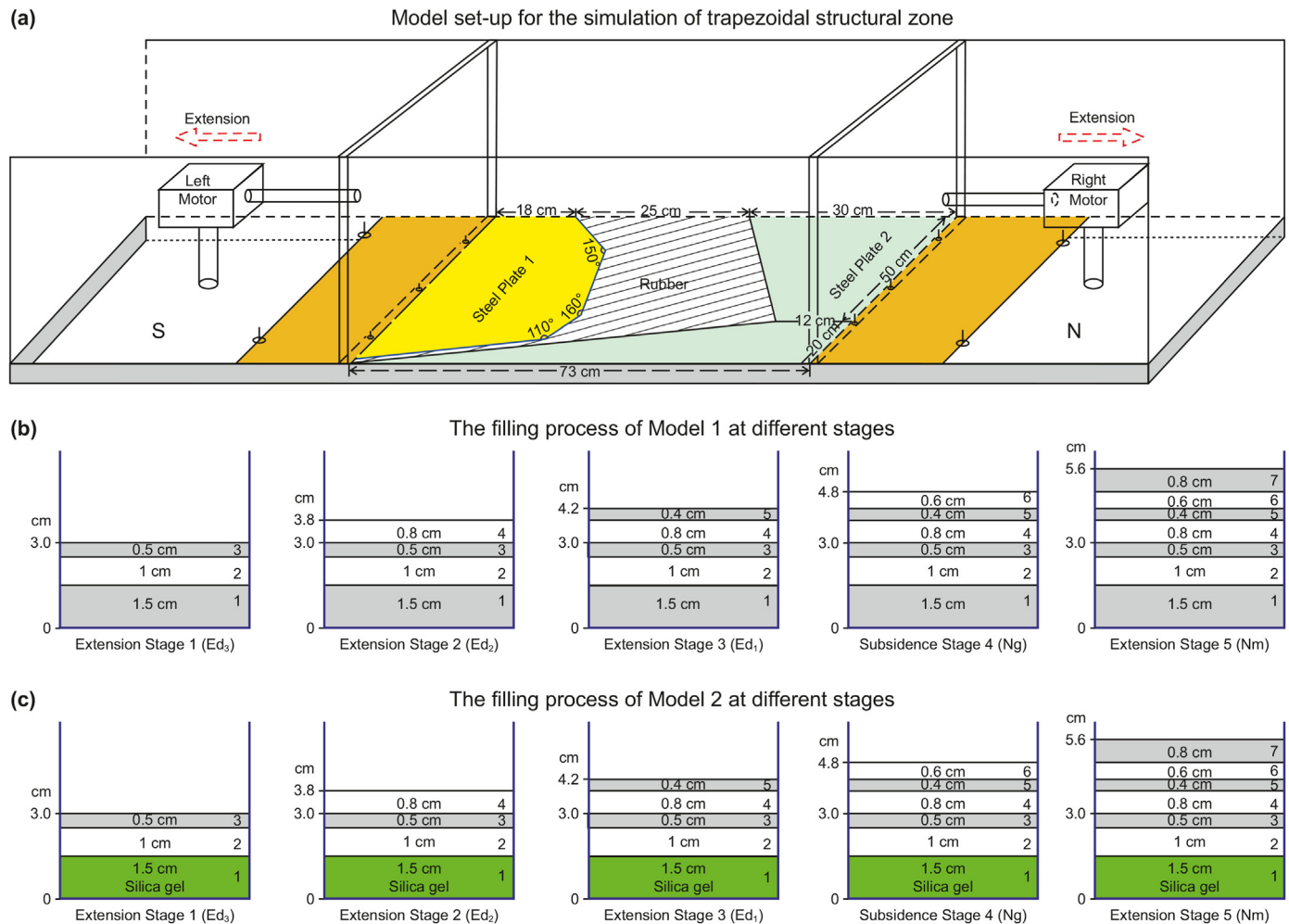
Fig. 9. Geometric shape and filling process of the experimental set-up. **(a)** Schematic diagram of the model set-up showing a 3D view of the deformation device and its components used to simulate the evolution of the trapezoidal fault zone during the Oligocene to Pliocene period. Schematic diagram of the filling process in different stages of **(b)** Model 1 and **(c)** Model 2. The base materials of the two models are different. The bottom of the Model 2 is filled with silica gel, and the material and thickness of the other layers are the same. The red arrow represents the extension direction of the device, and the deformed bottom is made of rubber.

Table 1
Kinematics of the models presented in this study.

Deformation stage	Extensional stage		Total model thickness, cm
	Extension direction	Total extension amount, cm	
Model 1	Sand basement		
1	Left-right (S–N)	2.0	3.0
2	Left-right (S–N)	2.5	3.8
3	Left-right (S–N)	3.0	4.2
4	Subsidence stage		4.8
5	Left-right (S–N)	5.5	5.6
Model 2	Silica gel		
1	Left-right (S–N)	2.0	3.0
2	Left-right (S–N)	2.5	3.8
3	Left-right (S–N)	3.0	4.2
4	Subsidence stage		4.8
5	Left-right (S–N)	5.5	5.6

stages of evolution.

4.2. Transensional fault system

Strike-slip faults are challenging to identify in sections because

their deformation is concentrated in strike displacement. This unique structure was identified in this study through the plan view analysis of the fault system. The faults of the FZ④ in Nm were categorized into two groups: Those directly vertically linked and dip synthetic with reactivated basement fault (Fig. 1(a)) at Es (linear

Table 2
Scaling parameters of the analogue model.

| Scaling parameter	Model	Nature	Model/nature ratio
Length l, m	0.01	500	0.5×10^{-5}
Density of sand ρ, kg/m^{-3}	c. 1450	c. 2700	0.54
Density of silica gel ρ, kg/m^{-3}	c. 929	c. 2200	0.42
Viscosity of silica gel	c. 1.2×10^4	c. $10^{-17}–10^{-19}$	$10^{13}–10^{15}$
Gravitational acceleration g, m/s^2	9.81	9.81	1
Stress σ, Pa			c. 2.7×10^{-6}
Grain shape	Well-rounded		
Grain size, mm	0.30		
Friction angle, °	c. 36	c. 40	0.9
Internal friction μ	0.73	0.84	0.86
Cohesion τ_0, Pa	100–140	10^7	$(1.0–1.4) \times 10^{-5}$
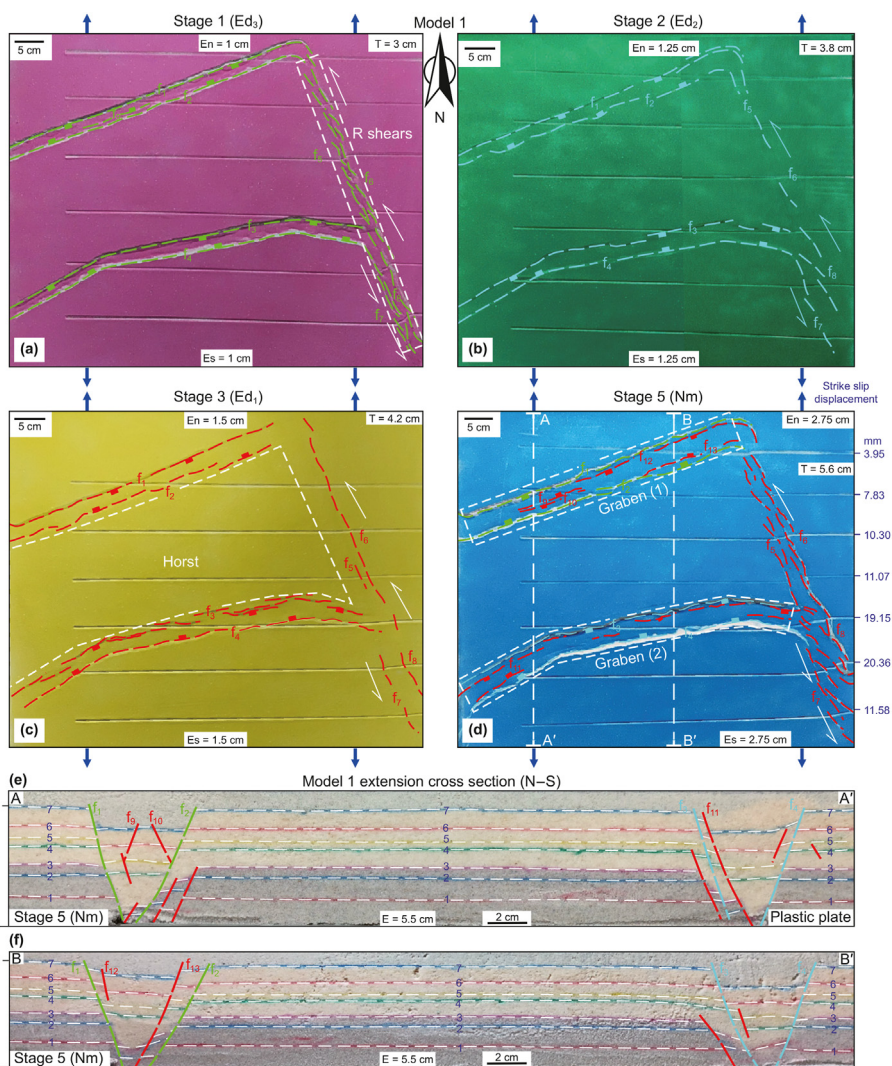
Fig. 10. (a)–(d) Top views (photographs and line drawings) of different stages of Model 1 showing the evolution of the structural zone at different extension stages. **(e)** and **(f)** N–S cross-section interpretations (photographs and line drawings) of the final stage of Model 1 representing the deformation styles (for cross-section locations, see Fig. 10(d)). Ed$_3$: third Mbr of the Dongying Fm in Oligocene; Ed$_2$: second Mbr of the Dongying Fm in Oligocene; Ed$_1$: first Mbr of the Dongying Fm in Oligocene; Nm: Minghuazhen Fm in Pliocene; En and Es represent the extension from the north and south direction; T represents the total thickness of the sand layer; and the blue arrow represents the direction of extension.

transtensional faults f$_1$–f$_7$ and arc-bending en-échelon splay faults in the Nm (green faults in Fig. 5(b)). The major strike-slip faults are oriented in the NW direction, and they exhibit a mostly straight geometry, with f$_6$ and f$_7$ bending as their strike gradually turns towards the NW and connects with the normal faults in FZ②. The direction of the splay faults primarily aligns in an EW direction, and

they constitute the transition zone between NEE and NW faults (Fig. 5(a)). Each transtensional fault presents an arc-shaped fault that protrudes to the north and overlaps in the south, resembling the shape of a horsetail structure (Woodcock and Fischer, 1986; Basile and Brun, 1999; Kim and Sanderson, 2006; Arfaoui et al., 2017). In the Es$_3$, a single major fault separates areas with
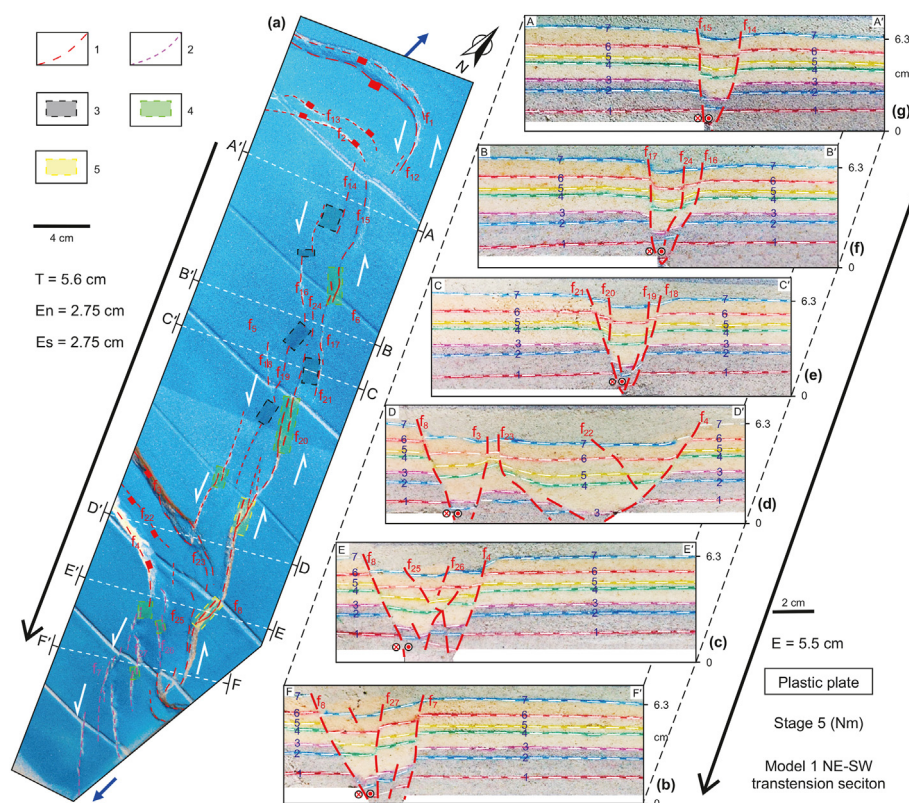
Fig. 11. Model 1 diagram of the transtensional fault zone. **(a)** Partially enlarged top view (photograph and line drawing) of the transtensional fault zone; **(b)**—**(g)** NE—SW cross-section of the final stage of Model 1 (photograph and line drawing), representing the deformation styles (for cross-section locations, see Fig. 11(a)). Abbreviations are the same as for Fig. 10. 1: R-shear; 2: intensely deformed R-shear; 3: isolated fault; 4: relay ramp; and 5: breached relay ramp.

significantly different topography, which is distinct from the complex deformation pattern in the Nm. Surface depth indicates the presence of pre-existing uplift variations in the terrain from north lower to south higher (Fig. 5(c)).

Seismic sections perpendicular to the fault strike (Fig. 7) were used to elucidate the detailed geometry of the transtensional fault system. Through plan combination (strike, number, and width of faults) and seismic interpretation, this transtensional fault system was subdivided into three segments (south, middle, and north). The south segment A, with a length of 4.72 km, is illustrated in Fig. 7(a)—(d). The major faults remained straight, and the linear continuations were f_1, f_4, and f_5. The increased complexity of caprock deformation results in continuous variations in the segments connected to the basal strike-slip fault. Therefore, the labels of the main transtensional faults within the caprock change. However, at deeper levels, they all converge into the same principal strike-slip fault. The dip angles of major faults were $70°-82°$ in deep strata and $56°-60°$ in shallow strata. The dip angles gradually decreased, and the vertical deformation was displaced. The narrow deformation zone has a width ranging from 3.45 to 4.85 km. The transtensional splay faults, in conjunction with the major faults, exhibited a high dip angle characteristic, distinguishing them from normal faults. This deformation formed a prominent negative flower structural style. The overall deformation zone shows steep and narrow characteristics.

The middle segment B (Fig. 7(e)—(g)), with a length of 6.84 km, had a western connection to the FZ③. The major transtensional faults f_3 and f_5 served as the boundary of the imbricated fan structure, whereas the dip angles in the sections became gentler than in the south segment, ranging from $70°$ to $75°$. The secondary faults that developed in the shallow layer (from the Ed to Nm) did

not overlap with the major faults and formed independent collapse structures (McClay, 1990) instead. Multiple secondary faults combined to form a composite "Y" shaped structural style. The linear transtensional fault was separated into two segments (f_3 and f_5) and might be connected by soft linkage. Connecting fault splays (f_{16}, f_{17}, f_{18}, f_{19}, and f_{20}) were curved and gradually curved into the major fault planes (f_3 or f_5), forming a continuous sinuous or slightly zig-zag fault geometry. Due to the predominant dip in the same direction (S) exhibited by the overstepping segments, the oversteps can be regarded as synthetic transfer zones.

The north segment C, depicts in Figs. 6(c), 7(h) and 7(i), has a length of 4.75 km and connects with the FZ② in the western part. Seismic interpretation reveals that the faults were symmetrically distributed in a conjugate pattern. The deformation zone was more expansive, measuring 10.2 km, with greater fault spacing. The splay faults of the FZ② overlapped with the major fault f_6 forming a negative flower structure in the caprock. The dip angles of the major faults continued to decrease to approximately $60°$. Although the negative flower structural style confirms the strike-slip component, the wider deformation zone and the conjugate fault combination indicate that the extensional component plays a more dominant role than that of the strike-slip component. Displacement transfer between strike-slip and normal faults commonly occurs through gradual modifications of fault orientations and slip vectors near the intersection zone. Consequently, the transtensional fault system exhibits a gradual increase in extensional component and a decrease in strike-slip component from south to north.

Regarding the kinematic characteristics of the transtensional fault system, a mechanism of left-lateral transtensional movement was established. In a pure strike-slip deformation scenario, narrow
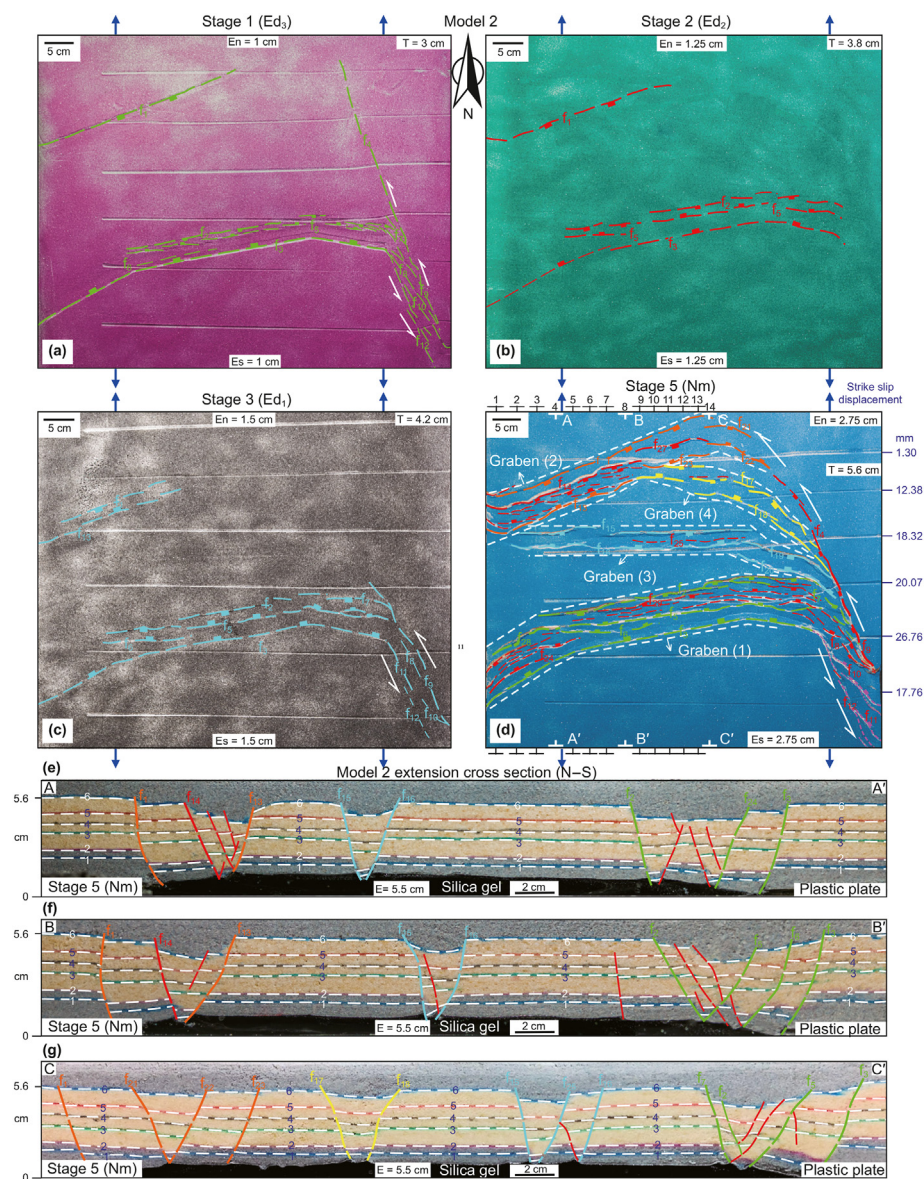
Fig. 12. **(a)**–**(d)** Top views (photographs and line drawings) of different stages of Model 2 showing the evolution of the structural zone at different extension stages. **(e)**–**(g)** N–S cross-section interpretations (photographs and line drawings) of the final stage of Model 2 representing the deformation styles (for cross-section locations, see Fig. 12(d)). Abbreviations are the same as for Fig. 10.

strike-slip displacement bends, such as R shear, R' shear, and PDZ, are formed. However, the width of the FZ④ increases gradually from south to north (2—5.2 km), and the number of faults decreases correspondingly (Fig. 7). This divergent fault combination has prominent extensional deformation components, whereas the linear distribution of major faults indicates strike-slip deformation components. Therefore, we identified this structure as a transtensional deformation with extensional and strike-slip components. Fault F_4 exhibited strong strike-slip movement in the Es_3, as evidenced by its nearly vertical fault morphology in Fig. 7(a)–(d). In the Es, due to the NW–SE extension in the basin, the NE-trending faults, F_2 and F_3 acted as the primary syn-rift faults. The structural map confirms this as the deepens side toward the fault plane (Fig. 5(c)). The fault F_4, acting as a transfer fault during the Es, adjusted the uneven extensional component along the fault F_3. This resulted in left-lateral strike-slip motion of the fault F_4. From another perspective, since the Ed, the N–S extension, oblique

interacting with the pre-existing uplift, has led to the development of unique geometric patterns in the overlying fault systems. The angle formed between the en-échelon splay faults and the linear transtensional fault in the termination zone indicates the left-lateral transtensional movement (Figs. 5(a) and 7).

5. Evolution of the transtensional fault system

We reconstructed the evolutionary process of the transtensional fault system from the initial extension of Paleozoic erathem to the reactivation during the Cenozoic according to the geological features along the N–N' section (Fig. 8). The reconstructed basement was mainly based on four pre-existing faults, i.e., F_{SB}, F_3, F_4, and F_{BGZ}, collectively forming two grabens. The central part was the paleo-uplift bounded by faults F_3 and F_4 (Fig. 8(a)). The Paleozoic strata may have undergone erosion at the paleo-uplift. The similar remaining thicknesses on both sides of the graben indicated stable
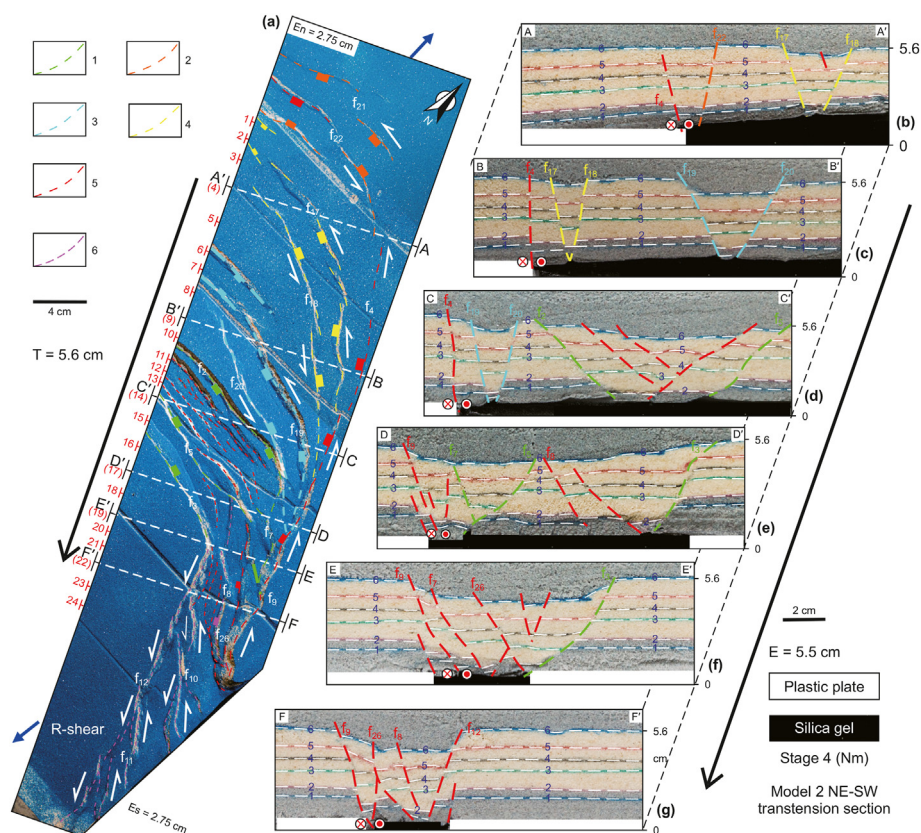
Fig. 13. Model 2 diagram of the transtensional fault zone. **(a)** Partially enlarged top view (photograph and line drawing) of the transtensional fault zone. **(b)**–**(g)** NE–SW cross-section of the final stage of Model 2 (photograph and line drawing), representing the deformation styles (for cross-section locations, see Fig. 13(a)). Abbreviations are the same as for Fig. 13. 1: Graben (1); 2: Graben (2); 3: Graben (3); 4: Graben (4); 5: Major fault; and 6: R-shear.

tectonic pattern during the Cratonic period. According to our seismic interpretation (Fig. 8), the paleo-uplift was inferred to be the highest in the southern segment of fault F_4, and it gradually flattened to the north. This paleo-uplift provided the geometric basis for the subsequent oblique extension. In the first stage of deformation (Fig. 8(b)), along the NW–SE extension during the Eocene, fault F_4 experienced a strike-slip solid effect. The domino fault pattern developed in the sedimentary centre on the north side. In the second stage of deformation (Fig. 8(c)), along the N–S extension in the Oligocene, the change in the extension direction caused the transfer fault F_4 to experience transtensional deformation, and numerous secondary faults developed in the grabens on the north and south sides. In the third stage of deformation (Fig. 8(d)), the fault activity became weaker, and few new faults developed. The Miocene uniformly covered the entire sag, thus comprising a post-rift thermal subsidence. We refined the deformation of the fourth stage, and more faults were developed during the Pliocene in the caprock. Some wedge thickening confirmed the activity of the faults in the late stage (Arrows in Figs. 6–8). Therefore, the fourth stage of deformation was defined as the structural reactivation of N–S extension. The reactive extension acted on fault F_4 to result in transtensional deformation. A distinct negative flower structure was formed in the southern segment (Fig. 7(a)–(d)).

6. Analogue modelling

To illustrate the tectonic evolution of the trapezoidal fault zone, we developed two analogue models to validate the evolution model (Fig. 8). We simplified the structure formed during the NW–SE

extension during the Eocene period, and designed it as a specific boundary, as the pre-existing structure during the Oligocene period. Two filling processes were employed to determine whether the unique geometry of the fault zone is related to the detachment of thick mudstones in the Eocene of the basement.

6.1. Experimental set up and kinematics

The analogue model of dimensions 73 × 65 cm included a sandbox simultaneously driven by motors on the north and south sides (Fig. 9(a)). The extension rate was maintained at 0.05 cm/min. A thin layer of elastic rubber cloth (thickness of 1 mm) was laid on the base of the model to ensure uniform extension. The model comprised two plates, namely Plate 1 and Plate 2, made of steel material with a thickness of 0.5 cm. Among them, Plate 1 comprised two parts: the west was a trapezoid with a length of 50 cm and a width of 30 cm, and the east was a trapezoid with a length of 20 cm and a width of 65 cm. The two parts shared 12 cm at the top of both the trapezoids. This geometry was used to simulate the geometric features of the boundary fault F_2. Plate 2 was a geometric structure 18 cm from the western boundary and 26 cm from the eastern boundary. This geometry was used to simulate the southern boundary of the fault, F_{SB} (Fig. 9(a)).

For Model 1, the experiment was conducted in five stages. In the first stage, loose sand layers with 1.5, 1.0, and 0.5 cm thicknesses were placed on the base of the model to simulate the sedimentary strata in the Eocene. The surface was marked with additional pink quartz sand (thickness of 0.02 cm), both sides were simultaneously extended, and the motor stopped when the extension reached 2 cm (Fig. 9(b)). In the second stage, a layer of loose white quartz sand
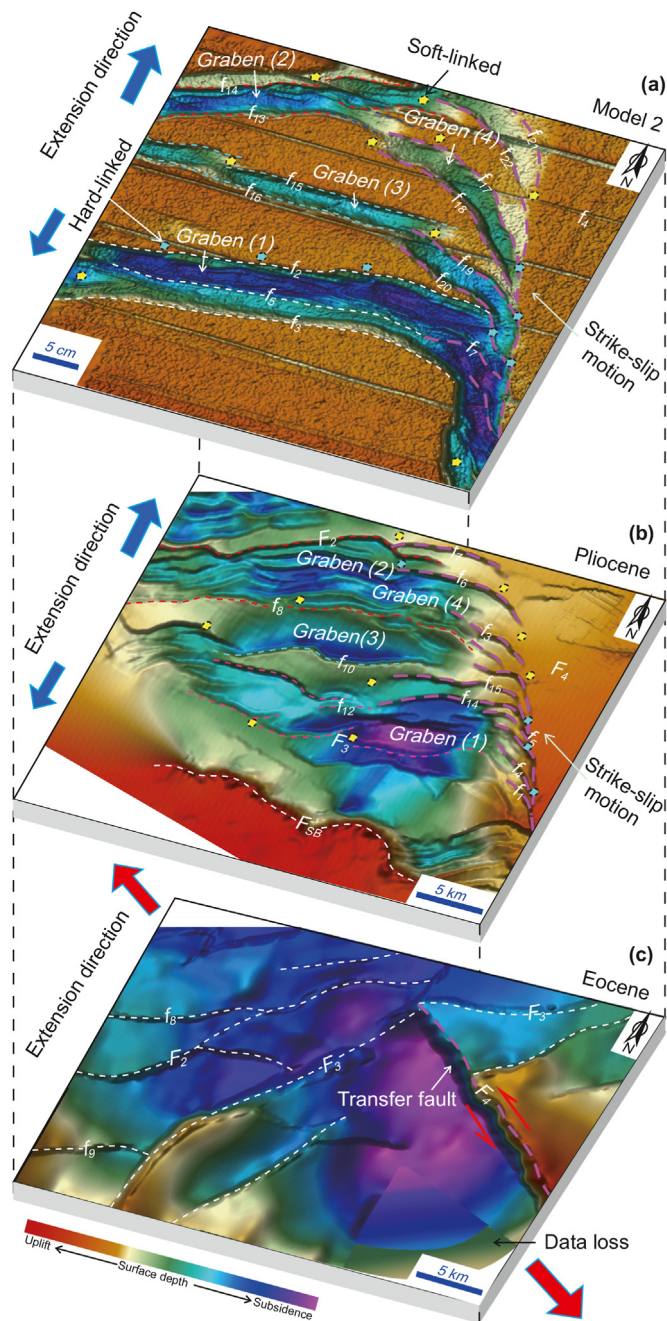
Fig. 14. 3D model diagram showing the comparison between experimental results and seismic interpretation results. **(a)** 3D display of the scanning results of Model 2 (Stage 5). **(b)** 3D display of the Pliocene seismic reflection of the trapezoidal fault zone indicating the main structural elements. **(c)** 3D display of the Eocene seismic reflection of the trapezoidal fault zone indicating the main structural elements. Fault names in **(a)** are same as in Fig. 12(d) and in **(b)** are same as in Fig. 5(a). The arrows indicate the extension direction.

with a thickness of 0.8 cm was placed on the deformed formation to simulate the sedimentary strata in Ed$_3$. Green quartz sand was placed as a marker layer. Then, the model was simultaneously extended by 0.25 cm on both sides, and the motor stopped (Fig. 9(b)). In the third stage, a layer of 0.4 cm thick loose white quartz sand was placed on top of the deformed strata, representing the sedimentary strata in Ed$_2$. Yellow quartz sand was placed as a marker layer. Subsequently, the model was simultaneously extended by 0.25 cm on both sides, and the motor stopped

(Fig. 9(b)). In the fourth stage, a layer of loose white quartz sand with a thickness of 0.6 cm was placed on the deformed strata, which represented the sedimentary strata in Ed$_1$, and red quartz sand was used as the marker layer. In the fifth stage, as the Ng was a subsidence period, 0.8 cm of loose quartz sand was placed to represent the Miocene sedimentary strata. Blue quartz sand was used as a marker layer. Next, the model was simultaneously extended by 1.25 cm on both sides, and the motor stopped (Fig. 9(b)).

The experimental stages of Model 2 are the same as those of Model 1. However, we placed a 1.5-cm-thick silica gel layer for the strata at the base of the model to replace the original 1.5-cm-thick sand layer (Fig. 9(c)). The upper sand layers and other experimental parameters remained unchanged. The total thickness of the deformed sand layer in the final stage of Models 1 and 2 was 6.4 cm. After all marker layers were laid, equally spaced marker line cuts were constructed to observe the development of strike-slip faults. A 0.8-cm-thick sand layer was laid on top of the final stage to cover the model and impregnate it with water. Continuous vertical sections were sliced and photographed at 3 cm intervals. N–S-trending sections in the model were selected for the extensional deformation zone, and NE–SW-trending sections perpendicular to the transtensional fault strike were selected for the transtensional deformation zone. All design parameters are listed in Table 1.

6.2. Scaling

The model described herein was scaled to the geometry, kinematics, and dynamics of the trapezoidal fault zone in the NPS. The geometric similarity is determined by a thickness ratio of approximately 1×10^{-5}; this finding implies that 1 cm of loose quartz sand in the model represents a 1-km-thick sedimentary layer in nature. The internal friction angle of loose quartz sand is $36°$, and its cohesive strength is 1.05 kPa. Additionally, according to the Coulomb fracture criterion, it is an ideal material for simulating the deformation of brittle sediments in the upper crust (McClay, 1990). The silica gel layer at the bottom of Model 2 has a viscosity of 1.2×10^4 Pa s and a density of 929 kg m^{-3}. Furthermore, silica gel exhibits Newtonian fluid properties at low strain rates; thus, it is often used to simulate plastic deformation of the upper crust (Weijermars and Schmeling, 1986; Rojo et al., 2020).

The kinematic similarity was obtained by simulating a model wherein sequence events follow the predicted evolution history of the NPS (Fig. 8). Based on our interpretation of the seismic data, we proposed and simulated the structural sequence relations of different sedimentary forms, that is, a five-stage evolution: four stages of N–S extension and one stage of subsidence (Fig. 9).

The dynamic similarity was fulfilled by simulating the physical properties of the sedimentary units of the fault zone using appropriate modelling materials. Thus, the intrinsic material properties, such as cohesion (τ_0) and the coefficient of internal friction (μ), needed to be approximated in the models and nature (Koyi and Petersen, 1993; Koyi, 1997). The angle of the internal friction of rocks in the upper crust (<10 km) is $40°$, on average (Koyi and Vendeville, 2003; Yu and Koyi, 2016), thereby yielding a coefficient of internal friction of 0.84. The internal friction angle of the uncompacted loose sand used in the models is $36°$, yielding a coefficient of internal friction of 0.73, considered proximate to that of the rocks in the upper crust. Additionally, cohesion (τ_0) was scaled based on the equality between the non-dimensional shear strength in the models and nature. This condition is indicated in Eq. (1):
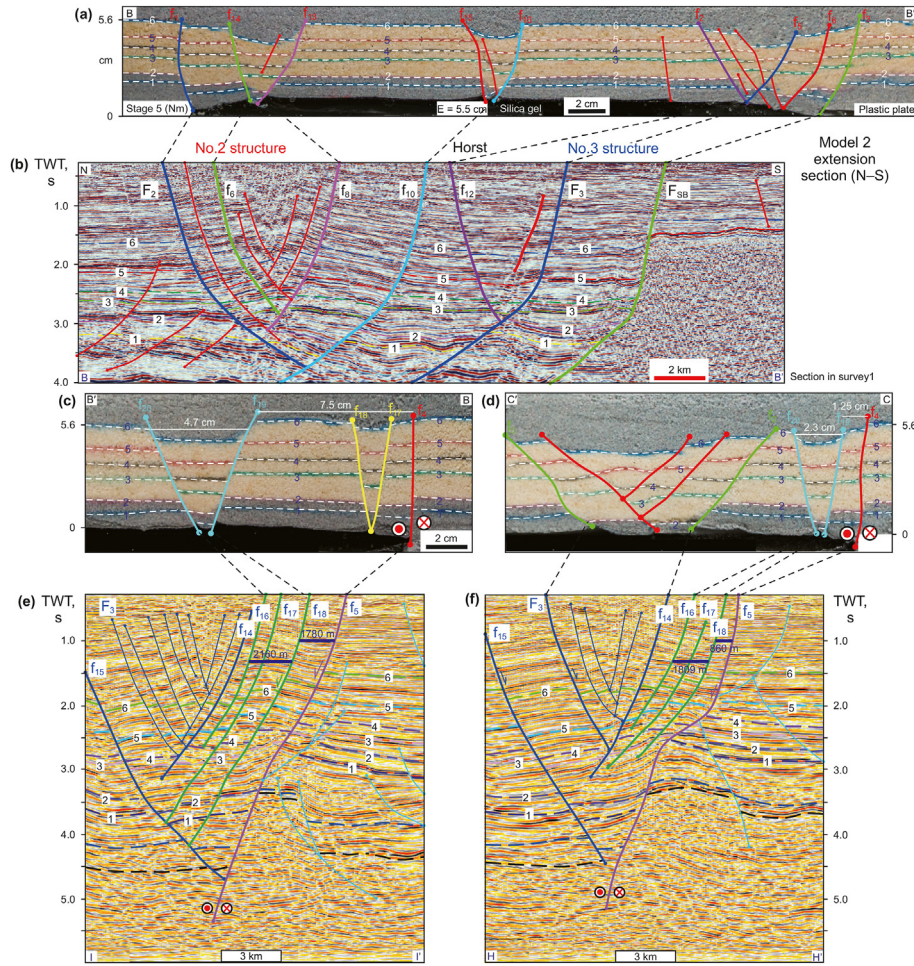
Fig. 15. Comparison between Model 2 results and interpretation of seismic sections across the trapezoidal fault zone. **(a)** Photograph and line drawings of the N–S cross-section in Model 2 (for location, see Fig. 12(d)). **(b)** Seismic interpretation section of the trapezoidal fault zone (for location, see Fig. 2(c)). **(c)** and **(d)** Photographs and line drawings of NE–SW cross-sections in Model 2 (for location, see Fig. 13(a)). **(e)** and **(f)** Seismic interpretation section of the FZ④ (for location, see Fig. 7(j)). Fault names in **(a)** are same as in Fig. 12(d), and in **(b)**, **(e)**, and **(f)** are same as in Fig. 5(a). Fault names in **(c)** and **(d)** are same as in Fig. 13(a).

$$\left(\frac{\rho g l}{\tau_0}\right)_{m} = \left(\frac{\rho g l}{\tau_0}\right)_{n} \quad\quad (1)$$

where, ρ is the density, l is the length, g is the acceleration owing to gravity, and subscripts m and n denote the model and nature, respectively. The non-dimensionless ratio is calculated for the model and nature using the shear strength of sedimentary rocks ranging from 1 to 10 MPa. The shear strength and density of the Clastic sediments are 10 MPa and 2550 kg m^{-3}, respectively (Yu and Koyi, 2016). The cohesion of the loose sand is approximately 100−140 Pa, and its density is 1550 kg m^{-3} (Table 2). These characteristics yield non-dimensional shear strengths (Eq. (1)) of 11−15 for the model and 25 for the natural setting. These two values, within the same order of magnitude, suggest that our models well approximated the dynamic similarity with their prototypes.

Following the scaling procedure (Ramberg, 1981; Weijermars and Schmeling, 1986), the scaling stress (σ^*) is given as follows:

$$\sigma^* = \frac{\sigma_{mod}}{\sigma_{nat}} = \rho^* g^* l^* = \frac{\rho_{mod} g_{mod} l_{mod}}{\rho_{nat} g_{nat} l_{nat}} \quad\quad (2)$$

The calculated σ^* is ~0.27 × 10^{-6}, and all the scaling parameters used in our models are listed in Table 2.

6.3. Model results

6.3.1. Model 1

During Stage 1 deformation of Model 1 with an extension of 2 cm, boundary faults f_1 and f_4 appeared first, followed by their anti-dip faults f_2 and f_3, which formed two complete narrow grabens. From south to north, a series of R shears, such as f_5, f_6, f_7, and f_8, developed (Fig. 10(a)). The strike-slip components of faults f_7 and f_8 were the largest in the south according to the misalignment of the marked lines. We named the linked R shears f_8 and the northern f_6 as the sequenced R shears for easy distinction. When Stage 2 extension reached 2.5 cm, no new faults formed. Here, faults f_5, f_6, f_7, and f_8 still exhibited strike-slip displacement, although a large amount of R shear was lacking (Fig. 10(b)). When the extension reached 3 cm, the top view showed no new faults, and the characteristics were similar to those of Stage 2 (Fig. 10(c)). In Stage 5, when the extension reached 5.5 cm, graben (1), defined by faults f_1 and f_2 on the north side, and graben (2), defined by faults f_3 and f_4 on the south side, were still present, and several secondary faults developed within these two grabens. A horst structure bounded by faults f_2 and f_3 was present in the centre. A series of R shears appeared in the east, and the width of the transtensional zone increased compared with that of Stage 1. The connection between the transtensional zone and the graben was developed along the
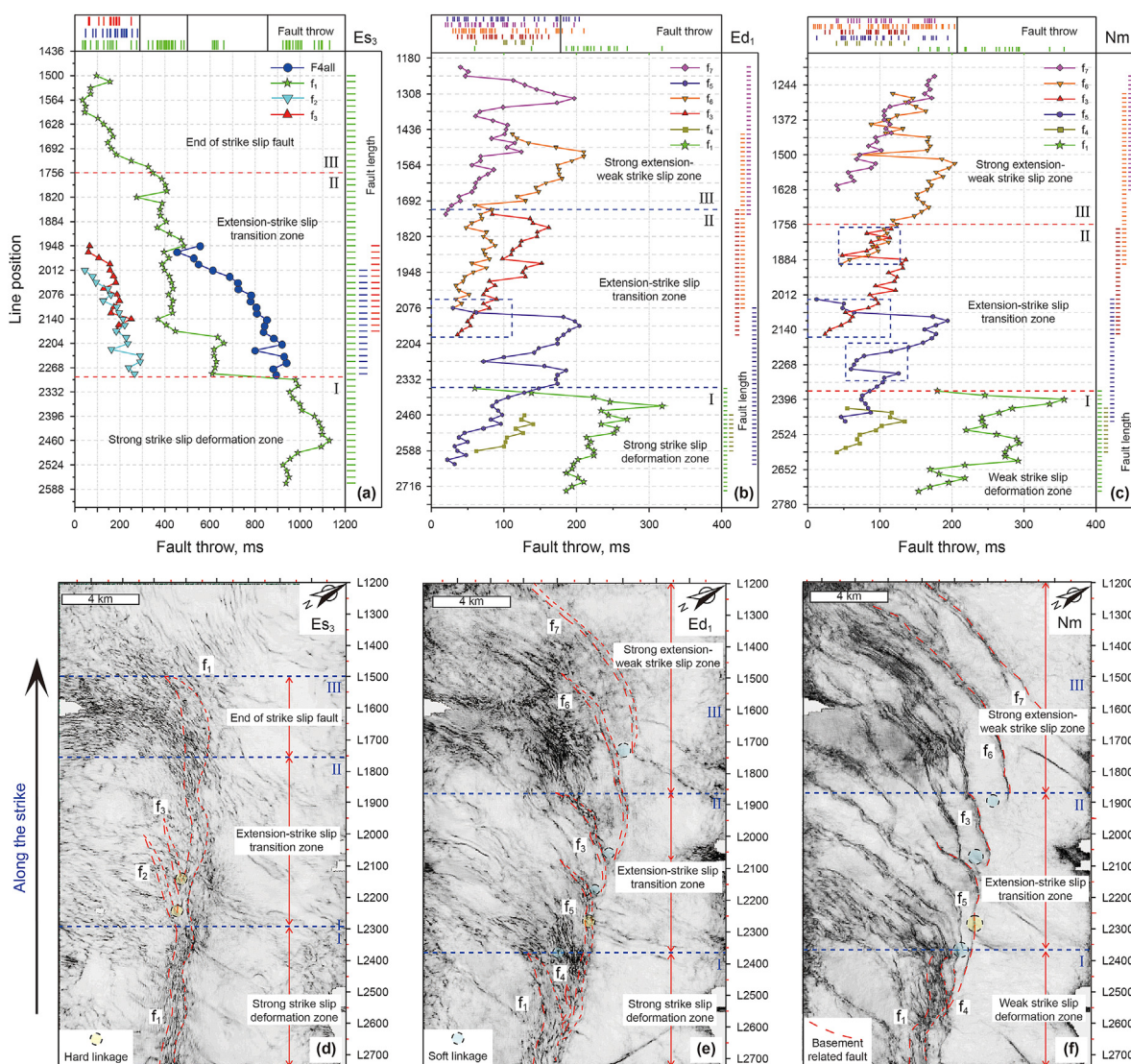
Fig. 16. Statistics and identification of faults in the transtensional fault system in three periods. **(a)**, **(b)**, and **(c)**: Fault throw statistics along the fault strike. **(d)**, **(e)**, and **(f)**: Coherence plan map along seismic interpreted horizons slices, identifying fault shape and linkage mode. The north direction of the coherent slice is the northeast direction of the figure. Statistics and plan maps correspond to the top and bottom, respectively. Es$_3$ (third Mbr of the Shahejie Fm in Eocene), Ed$_1$ (first Mbr of the Dongying Fm in Oligocene), and Nm (Minghuazhen Fm in Pliocene).

eastern ends alone of the two grabens, and the assemblage of the extensional imbricate fans did not appear (Fig. 10(d)).

The N−S cross-section of Model 1 showed that several opposing secondary normal faults, f$_9$ and f$_{10}$, were present between graben (1) bounded by faults f$_1$ and f$_2$. Two early normal faults developed at the bottom of fault f$_2$, which terminated in the No. 4 white sand layer (Fig. 10(e)). This result indicated that the formation of normal faults alternated from the inside to the outside, and the width of the later developed graben increased. A similar phenomenon was observed at the bottom of the right-side fault f$_3$. Faults f$_3$ and f$_4$ jointly constituted the right side of the graben (2) boundary. All these faults exhibited a specific syn−sedimentary phenomenon, especially the boundary faults f$_1$, f$_2$, f$_3$, f$_4$, and f$_{11}$ (Fig. 10(e)). The phenomenon in Fig. 10(f) was similar to that in Fig. 10(e). The depth of graben (1) on the south side was greater than that of graben (2) in the north. Furthermore, the default southern model boundary was nearly E−W and maintained a large angle (80°) with the N−S extension direction, which explains the presence of stronger sediments (Fig. 9(a)).

A partially enlarged top view (photograph and line drawing) of the transtensional zone of Model 1 showed the plan deformation in detail (Fig. 11(a)). This transtensional zone manifested as an intense strike-slip deformation, paired with en-échelon-like R shears. The dislocation data of the marking line revealed that the strike-slip component from south to north gradually weakened until the northern faults f$_1$, f$_2$, f$_{12}$, and f$_{13}$ formed an arc-shaped bend, which connected the ends of the transtensional faults with the normal faults. The Model 1 NE−SW cross-section displayed a narrow and shallow graben formed by the R shears (Fig. 11(b)). Faults f$_{14}$ and f$_{15}$ were approximately upright, and more displacement was transmitted through strike displacement. Fig. 11(c) and (d) displayed the cross-section shape of the relay ramp. Two relay ramps were present among faults f$_{18}$, f$_{19}$, f$_{20}$, and f$_{21}$, with a small drop for transmitting the fault throw (Fig. 11(d)). The cross-graben sections (Fig. 11(e)) f$_3$, f$_4$, f$_8$, and f$_{23}$ constituted two grabens, with faults f$_3$ and f$_{23}$ forming a horst in the middle. In Fig. 11(f) and (g), intense strike-slip deformation is present under the two pre-set boundaries. Secondary faults f$_{25}$ and f$_{26}$, developed in the graben and
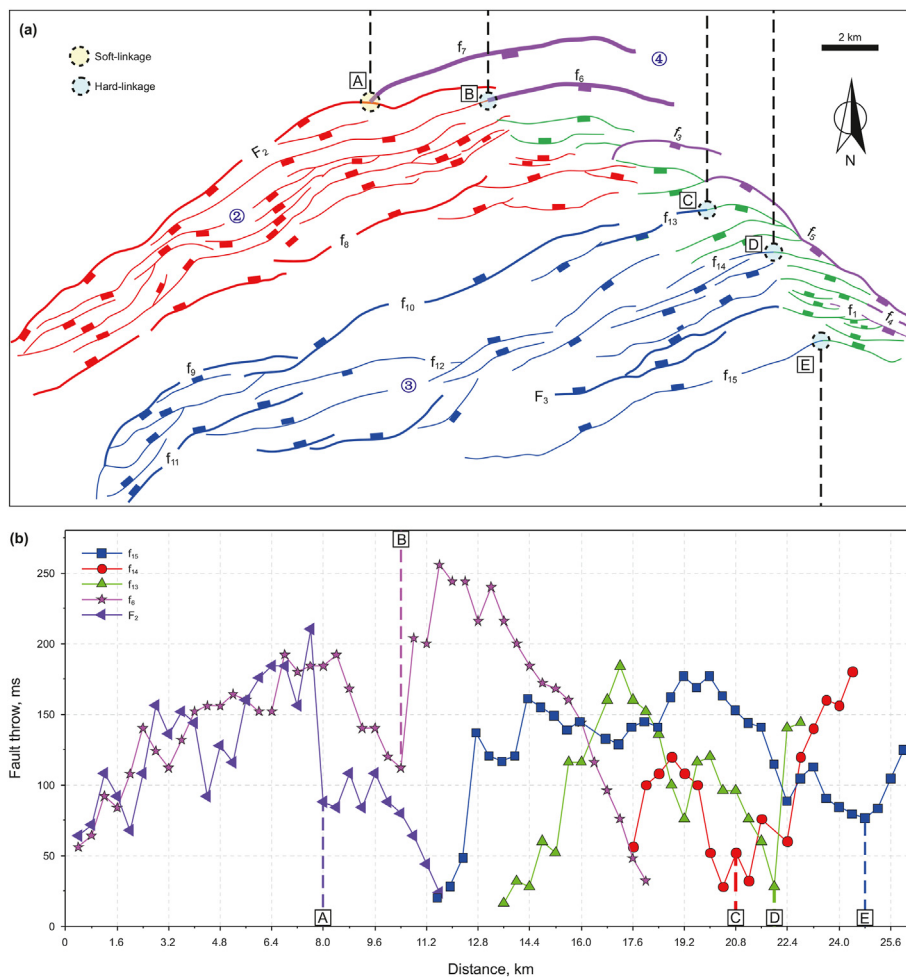
Fig. 17. Fault throw statistics of normal and transtensional faults. **(a)** Structural zone plan map; legend consistent with Fig. 5(a). **(b)** Plot showing the fault throw statistics of the five faults.

were bounded by faults f_4 and f_8. Two independent grabens appeared in the 1, 2, and 3 sand layers, indicating that two R shears had developed. An increasing number of R shears developed in the south with a widening relay ramp, which suggested that an extension effect was experienced. The secondary fault f_{27} developed in the graben was bounded by faults f_7 and f_8. Fig. 11(a) exhibited the relay ramp between the faults. We divided the relay ramp into isolated, mature, and wrecked stages (Peacock and Sanderson, 1994). Fault f_8 appeared as a continuous and curved strike-slip fault where breached ramps occurred, and secondary faults converged directly on fault f_8.

6.3.2. Model 2

This study provided the final top view alone of each extensional stage to facilitate the presentation of the conclusions. For more data, see the online supplementary materials (GIF for the deformation process). When Model 2 was extended to 2 cm in Stage 1, fault f_1 appeared along the boundary in the north. In the south, the graben (1) was bounded by faults f_2 and f_3, and the secondary faults f_5 and f_6 were present within it. A series of en-échelon-like R shears f_7–f_{12} generated in the southeast, and the strike-slip fault f_4 developed in the northeast (Fig. 12(a)). When the extension reached 2.5 cm in Stage 2, the graben (1) in the south still bounded by the faults f_2, f_3 further extended, and the fault f_1 existed in isolation (Fig. 12(b)). When the extension reached 3 cm in Stage 3,

the southern graben (1) was fully developed. The fault f_{13} appeared in the north, and the fault f_1 formed the NE-trending graben (2). The strike-slip deformation zone appeared in the southeast, which consisted of faults f_8–f_{11} (Fig. 12(c)). A complex structure formed when the extension reached 5.5 cm in Stage 5 (Fig. 12(d)). Different coloured faults were used to denote the entire graben. In the north, the NE-trending graben (2) was bounded by faults f_1 and f_{13}, and the secondary fault f_{14}, developed in the interior. In the central part, where no boundary faults were set, E–W trending faults f_{15} and f_{16} developed to form the graben (3), and the secondary fault f_{25} was formed within the graben. The large graben (1) bounded by faults f_2 and f_3 in the south comprised some secondary faults, such as f_5, f_6, and f_{24} (Fig. 12(d)). Furthermore, a convergent strike-slip deformation zone developed in the east, and the displacement of the marking line indicated that the strike-slip component gradually decreased from south to north (26.76 cm−1.3 mm). For convenience, we classified the continuous strike-slip boundary fault as fault f_9 and the scattered strike-slip boundary fault as fault f_4. The grabens gradually curved in an arc-shaped in the east, and a relay ramp connected the grabens. Vertical and strike displacements were transmitted through the ramp slope and ramp dislocation, respectively. The graben (1) was categorized into two grabens, with faults f_{21} and f_{22} and faults f_{17} and f_{18} as the respective boundaries. The graben formed by faults f_{17} and f_{18} was called graben (4), and that formed by faults f_{21} and f_{22} remained as graben (2) (Fig. 12(d)).
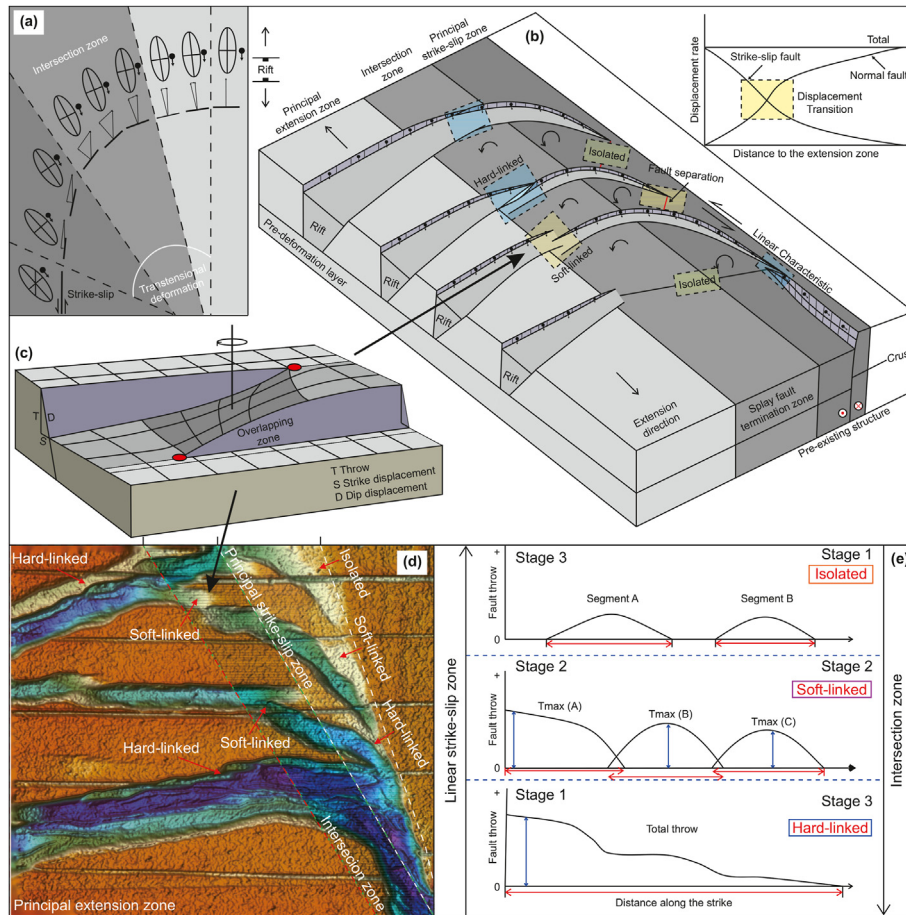
Fig. 18. Transtensional fault linkage evolution model. **(a)** Incremental horizontal strain ellipses illustrating principal horizontal shortening and extensions across the deformation zone (modified after Mouslopoulou et al., 2007). **(b)** 3D model of the transtensional fault linkage evolution in different principal deformation zones. The curve graph illustrates the relationship between the strike-slip displacement rate and the extension displacement rate. **(c)** 3D model of the rotational relay ramp in the overlapping zone (modified after Fossen and Rotevatn, 2016). **(d)** 3D stereogram of the linkage process of the transtensional faults (result in Model 2). **(e)** Plot showing the transtensional evolution statistics: fault throws along strike statistics.

These curved grabens completed the transition from extension to strike-slip.

The N−S cross-section of Model 2 displayed (Fig. 12(e)) three grabens. The graben (2) was formed by faults f_1, f_{13}, and f_{14}. The secondary faults within faults f_{13} and f_{14} cut each other. The graben (3), formed by faults f_{15} and f_{16}, was narrower than the graben (2), indicating that the graben developed rapidly. The graben (1), formed by faults f_2, f_3, and f_{24}, also exhibited two early anti-dipping faults, which terminated in the No. 6 white sand layer. More secondary faults developed in the footwall of fault f_3 in the graben (1), as shown in Fig. 12(f). The relay ramps between faults f_3, f_5, and f_6 were adjusted for the increased vertical displacement, resulting in no large fault throws (0.9−6.4 mm). The fault f_5 cut the secondary fault, forming an X-shaped structure. The graben (4), bounded by faults f_{17} and f_{18}, was shown in Fig. 12(g). The grabens (2) and (4) were extremely shallow, in sharp contrast to grabens (1) and (3), which illustrated heavy subsidence in the south. This finding indicated that the two grabens were in the extension−strike-slip transition region, and more displacements were transmitted by the relay ramp dislocation (Fig. 12(d)).

A partially enlarged top view (photograph and line drawing) of the intersection zone of Model 2 was used to demonstrate the deformation plan (Fig. 13(a)). The arc graben gradually converged to strike-slip faults f_4 and f_9, and the graben closer to the strike-slip fault became narrower and the strike-slip fault eventually

merged. The weakening of the northward strike-slip may cause an undeveloped fault f_4 to disappear. This observation explained the reason for graben (2) not converging into the fault f_4. Under the simultaneous actions of the two preset boundaries in the south, an apparent strike-slip deformation occurred (Fig. 13(a)), and various en-échelon-like R shears, f_{10}, f_{11}, and f_{12}, were present; however, they were not close to the preset boundary. Several wide relay ramps (average length 5.56 cm, width 1.41 cm) developed between them, which verified the presence of an extension and indicated that the extension caused the R shear arrangement to be highly dispersed in the extension direction. The NE−SW cross-section displayed the convergence process of the arc-shaped graben to the boundary strike-slip faults (Fig. 13(b)−(e)). The strike-slip segments fault f_4 and f_9 were sub-vertical to steeply dipping, with a rake of 76°−85° accommodating a minimal dip-slip (Fig. 13(b)−(e)). The connecting splays exhibit a continuous, arc-shaped fault plane as they intersect with the major fault planes. The strikes of the connecting faults range from 95° to 130° (up to 165°) in a clockwise direction relative to the major strike-slip segments. The dip angle varies from 55° to 70°, although it can locally be 85°. The dip and strike orientations show systematic variations in relation to the main faults, with similar strike angles observed for larger dip deviations (Fig. 7). The connecting faults demonstrate oblique sinistral-normal or pure normal kinematics. The ratio of dip-slip and strike-slip components varies with the

strike of the connecting faults, with larger strike deviations associated with larger rake angles. The graben (4) decreased in width and depth as it approached the strike-slip fault f_4. The fault dip also considerably increased (Fig. 13(b)). The grabens (1) and (3) also exhibited consistent characteristics (Fig. 13(c)−(e)), and they gradually disappeared and converged into strike-slip boundary faults, f_4 and f_9, respectively. The graben subsidence near the strike-slip boundary faults was minimal, and a strike-slip component replaced the dip-slip displacement. As the strike-slip component increased, the extension component decreased. Fig. 13(f) showed the highly deformed ends of the transtensional zone. Faults f_3 and f_9 were the boundaries of the graben, within which the secondary faults, f_7 and f_{26}, developed. The graben shown in Fig. 13(g) was narrow and had no relay ramp. Additionally, the fault throws of fault f_{12} increased considerably. Faults f_8 and f_{26} had secondary faults inside.

7. Discussion

7.1. Comparison among modelling results and nature

Models 1 and 2 exhibit analogous structural evolution to the trapezoidal fault zone. Nevertheless, Model 1 was devoid of continuous strike-slip boundary faults and an extension−strike-slip transition, a significant departure from natural conditions (Fig. 10). Brittle oblique extension exclusively generates narrow and dispersed fault segments, forming shear zones without linkage to normal fault systems aligned with the stress field. In the presence of a detachment layer in the basement, pre-existing structures undergo oblique extension, leading to the formation of arched en-échelon arrays in the overlying strata. This aligns principally with the current methodology. This outcome further suggests the indispensability of the detachment layer from the Eocene in the formation of transtensional fault systems. The detachment layer transmits a substantial amount of strain, leading to a more tightly coupled interaction between fault segments.

The distinct characteristics of the four grabens (marked in Fig. 14) and the lateral en-échelon arrangement of the transtensional faults provide compelling evidence that supports the close resemblance of Model 2 to the natural scenario. The millimetre-scale laser scanning result depicted the depth reduction in the intersection zone from south to north and a progressive reduction in settlement closer to the principal strike-slip zone (Fig. 14(a)). The simulation results proved that the constraint boundary formed by the faults F_{SB} and F_4 is the geometric condition for the intense strike-slip deformation of the southern segment. The strike-slip movement of the two plates intensifies the strike-slip component. Similarly, this phenomenon could also be attributed to the inherent topographic features, where, under the same strain field, the ancient topography exhibits a south-high to north-low pattern. Consequently, the northward strike-slip motion gradually weakens over time (Fig. 14).

The stress concentration on a pre-existing fault leads to fault reactivation, with strike-slip movement occurring when the extension direction aligns with the fault strike (Henza et al., 2011). In the Eocene, a substantial strike-slip deformation occurred when the NW−SE extension direction was nearly aligned with the strike of fault F_4, which served as a transfer fault by transmitting displacement to fault F_3 (Fig. 14(c)). As the extension direction and the strike of fault F_4 became increasingly misaligned in the Pliocene, the FZ④ showed extension and weakened strike-slip effects (Fig. 14(b)). In the Pliocene, subsidence led to the deposition of a considerable amount of strata, resulting in the increased scale of the rolling anticline under extension and eventual hanging wall collapse (Figs. 6−8 and 15). This phenomenon caused the formation

of numerous splay faults that overlapped in the same or opposite directions, resulting in a complex negative flower structure. However, these structures primarily developed at the bottom of the Oligocene; in contrast, the penetration was limited in the Eocene due to the thick mudstone layer deposited at the time, impeding the downward propagation of faults. On the plan view, these arc faults formed a horsetail splay stacked one after the other in the strike-slip termination zone (Fig. 14(b)). Continued extension caused the normal faults to grow and eventually connect with the transtensional faults in the intersection zone.

At the 5.5-cm extension, the structures formed by faults f_1, f_{14}, f_{13}, f_{16}, f_2, f_5, and f_3 in the simulated sections well corresponded with faults F_2, f_6, f_8, f_{10}, f_{12}, F_3, and F_{SB} in seismic sections, respectively (Fig. 15(a) and (b)). The transtensional faults f_{14}, f_3, f_{16}, f_{18}, and f_5 correspond well with the faults f_5, f_2, f_{20}, f_{19}, and f_4 in the simulation sections, respectively (Fig. 15(d) and (f)). The graben (3) adjacent to the major fault f_4 became narrow (4.7−2.3 cm), which is similar to the narrowing process of the stepped fault composed of f_{14} to f_{18} in the seismic section (2160−1809 m). The distance between faults f_4 to f_{19} (7.5−1.25 cm) and f_5 to f_{18} (1780−860 m) indicates the process of approaching the strike-slip fault. The faults that narrow gradually in the section and eventually bend in the plan are identified as transtensional. The closer these faults are to the major strike-slip fault, the smaller their dip displacement becomes. Eventually, these faults converge into a major strike-slip fault and merge together. This process reconstructs the arc bending process of the secondary faults at the end of the extensional imbricated fan. However, there are also some differences in section correlation. While several secondary faults formed negative flower structural styles in the seismic section, they did not exist in the simulated section. This observation could be because the simulation experiment did not include the extension stage from the NW−SE direction of the Eocene, which is responsible for the strong strike-slip stage of fault F_4 The present transtension deformation may not be enough to develop the negative flower structure.

Furthermore, this work is also limited by its consideration of multi-phase extension in different directions (Henza et al., 2010). The sandbox analogue modelling followed the syn-sedimentary process, although our experimental stage started from the N−S extension, overlooking the first NW−SE extension stage. This limitation led to the absence of apparent syn-sedimentary phenomena in the rapid rifting of NE-trending faults, which may not correspond well with the scenario in Fig. 10. Oblique extension and pre-existing structure are significant evidence for horsetail splay faults. But this does not overwhelmingly support the impact of strike-slip displacements in first stage on the second stage fault formation during the missing NW−SE extensional stage. Owing to the complexity of the inversion modelling process, the distances between adjacent units in the modelling process do not precisely match with those observed in nature. However, their similar structures suggest that the fault zone has undergone the same tectonic evolution as that in the experiments.

7.2. Fault linkage evolution in the transtensional fault system

Fault intersections are an essential feature for the evolution of all fault systems, and are generally accommodated by soft linkage-hard-linkage. (Exadaktylos et al., 2003; Soliva and Benedicto, 2004; Morley, 2017; Wyrick et al., 2011; Fossen and Rotevatn, 2016; Zwaan et al., 2020). Strike-slip faults exhibit an isolated-overstep accumulation−stepped growth curve. The T-D curve on transtensional faults can be used to confirm the nature of linkage of transtensional faults in different stages.

Our statistics focused on the major strike-slip faults of the FZ④ (f_1−f_7). The fault plan combination was performed according to the

coherent slice and seismic interpretation, and the fault T-D curve was completed according to the fault location. The plan and section diagram exhibited segmental deformation characteristics, which can be divided into three structural segments: the north, middle, and south segments (Figs. 7 and 16). According to its geometric characteristics, we divided the fault zone into three segments and observed that the characteristics and scope of each segment can be refined.

In the Es_3, according to the fault T-D curve (Fig. 16(a)), southern segment I (Fig. 16(a) and (d)) represented the strong strike-slip deformation zone. The fault f_1 had a considerable fault throw ranging from 900 to 1100 ms, with an average throw of 1009 ms (Appendix B: Supplementary Table 1). The highest throw was found at the and the throw decreased towards north rather than toward the lateral tips. This finding indicated that major fault throw was significantly associated with pre-existing geomorphological differences (Figs. 5 and 16(a)). Middle segment II (Fig. 16(a) and (d)) represented the extension−strike-slip transition zone, where fault throws of fault f_1 rapidly decreased from 980 to 446 ms (Appendix B: Supplementary Table 1). As a result of fault throw compensation, faults f_2 and f_3 developed (Fig. 16(d)). A section of a fault remained, causing secondary faults to develop and transfer the displacement onto itself, which led to sidewall rip-outs (Kim and Sanderson, 2006). Northern segment III (Fig. 16(a) and (d)) represented the end of this pre-existing strike-slip fault, intersecting the NE-striking FZ②, and the fault throw suddenly decreased from 346 to 250 ms. The drop in the fault throw to zero and the disappearance of the banded reflections on the coherent slices marked the end of the strike-slip fault.

In the Ed_1, fault f_1 was observed only in the southern segment I (Fig. 16(b) and (e)) with an average throw of 210 ms, which was much higher than the 95 ms average throw of other faults. We postulated that this region was the intense strike-slip deformation zone during this period. New faults f_4 and f_5 emerged in the southern segment, which shared the considerable fault throw of fault f_1. Compared with the Eocene, more faults were present in the southern segment, forming a fault zone rather than a single fault (Fig. 16(e)). Middle segment II (Fig. 16(b) and (e)) corresponded with the transformation of the FZ④, where faults f_3, f_5, and f_6 developed. The throw of this segment was reduced to 28−204 ms, with an average throw of 101 ms (Appendix B: Supplementary Table 1). Consequently, the faults became soft-linked, although the distance between them was minimal. Here, the faults f_3 and f_5 remained hard-linked. Arc bends all converged towards an oblique boundary. South segment III (Fig. 16(b) and (e)) represented the substantial extension with the weak strike-slip zone, where the distance between faults f_6 and f_7 was large and curved towards the north. This distance represents fault bending at the termination zone of splay faults, which is essentially the termination zone of a strike-slip fault (Woodcock and Fischer, 1986; Basile and Brun, 1999; Gabrielsen et al., 2001; Kim and Sanderson, 2006; Arfaoui et al., 2017). The average fault throws of faults f_6 and f_7 increased to 106 ms, which is much larger than those (79 ms) of the middle segment faults f_3 and f_5. The arcuate bending to the north and more enormous fault throws suggested that the N−S extension altered these faults (Fig. 16(b) and (e)).

In the Nm, the fault geometry was highly curved and dispersed, and the faults were no longer interconnected. Instead, the strike-slip displacement was eventually mediated by dip-slip faults. Here, fault f_1 was present in the south segment I alone (Fig. 16(c) and (f)), where the average fault throw remained 235 ms, which was significantly higher than those (84 ms) of the other faults (Appendix B: Supplementary Table 1). A large fault width was maintained in the coherent slices, and several faults converged to this large fault (Fig. 16(f)). This region could be considered as an intense strike-slip deformation zone. Middle segment II (Fig. 16(c) and (f)) was the extension−strike-slip transition zone. Although the distance between faults f_3 and f_5 was wider than that in the Oligocene (Fig. 16(f)), a soft linkage was still present, as indicated by the fault throw (Fig. 16(c)). The southern ends of the secondary faults maintained the oblique alignment and converged in the SE direction. The end of the soft linkage of faults f_3 and f_6 denoted the entry into the strong extension with the weak strike-slip zone (south segment III of Fig. 16(c) and (f)). Fault f_3 showed an abrupt change in fault throw, indicating the presence of new-born fault development of a hard linkage, resulting in the formation of a long, arc-shaped fault. The faults were substantially enlarged towards the north, and no notable fault throw correlation existed between faults f_6 and f_7 (Fig. 16(f)). Simultaneously, the increase in average fault throws from 32 to 121 ms of these two faults suggested that their activity was greatly enhanced by the N−S extension (Appendix B:Supplementary Table 1). However, the ends of the faults f_6 and f_7 still converged towards the SE direction, which proved that they were part of the transtensional splay fault.

Gradual bending of the transtensional faults led to the connection of the NE-trending fault ends with the FZ② and FZ③. T-D curves (Fig. 17) validated this linkage process, though it was challenging to identify them from the plan view. Statistical analyses indicated that the normal faults of the FZ② and FZ③ were connected to the transtensional faults through segmental growth (Fig. 17(b)). The sudden decrease in fault throw indicated complex linkage between adjacent normal faults, as observed for f_6, f_{13}, f_{14}, and f_{15} (B, C, D, and E points in Fig. 17, respectively). The relay ramp rapidly transmitted dip displacement, revealing the presence of soft linkage, as observed for f_7 with fault F_2 (A point in Fig. 17). These linkage points were located where the fault strike changed.

The fault linkage evolution model in oblique extension on pre-existing structures (Fig. 18), initially proposed based on seismic interpretations has gained further realism and reliability through validation in analogue modelling. The linkage process of transtensional faults resulting from oblique extension more closely resembles the growth process of normal faults. The intersection zone between strike-slip and normal fault systems is characterised by significant changes in their geometric features. The intersection zone of transtensional fault system can exhibit a range of strike orientations, from sub-parallel to sub-perpendicular (Fig. 18(b)). The principal fault system can be either strike-slip or extension, but its strike orientation undergoes significant changes. The observed variations in fault strike, dip and throw suggest that the two fault systems exhibit similar geometric characteristics in the intersection zone, indicating a shared kinematic background of the faults (Fig. 18(b)). In the intersection zone between strike-slip and normal faults, the orientation of principal incremental strain axis applied to the fault must change by 90° for synchronous slip. However, due to the constraints imposed by pre-existing structures (Figs. 1(a) and 18(a)) that do not intersect at 90°, the resulting slip vectors of the individual components are inevitably non-parallel. To achieve deformational stability, a greater amount of displacement is accommodated through internal deformation (Mouslopoulou et al., 2007). Assuming that the slip vectors in the intersection zone are already parallel, the movement can be directly accomplished through block translation, without the formation of relay ramps or curved faults. Therefore, in transtensional deformation intersection zones, the slip vectors must transition from nearly horizontal to obliquely parallel within the fault intersection zone. The schematic diagram illustrates the deformation process (Fig. 18(b)).

Simulation experiments have confirmed that in cases of synchronous activity between strike-slip and normal faults, there is displacement transfer between the faults, consistent with kinematic consistency in fault evolution. The displacements encompass

both along-strike variations and along-dip slips. In the transtensional fault system, the slip vectors between faults can be arranged in a horizontal (0−20°), oblique (20−70°), or vertical orientation (70−90°) (Mouslopoulou et al., 2007). The oblique zone can be named as transtensional deformation zone (Fig. 18(a)). Along-strike displacements are accommodated through the linear surface of the principal strike-slip zone (Fig. 18(b)), the progressive bending of splay faults, and the formation of relay ramps occur. Under persistent oblique extension, relay ramps underwent rotation to accommodate increased displacements between fault segments, ultimately resulting in the breach of the relay zone. Laser scanning reveals that the simulation experiment can also be distinctly categorized into principal extension zone, intersection zone and principal strike-slip zone (Fig. 18(d)). In the transition zone, a substantial amount of strike-slip displacement is accommodated through the misaligning of relay ramps. The hierarchical elevation differences highlight the segmented nature of faults in the principal strike-slip zone. In the fault overlap zone, displacement transfer becomes more pronounced, leading to more complex deformation (Peacock and Sanderson, 1994; Gawthorpe and Leeder, 2000; Fodor, 2007; Fossen and Rotevatn, 2016; Zwaan et al., 2020). Due to the challenges in quantitatively analysing simulation experiments, we cannot derive a comprehensive quantitative strain formula. However, based on observed offset markers, it can be inferred that under the interaction of two displacement fields, oblique extension occurs, with regions of higher strike-slip rates than extension rates (Fig. 18(b)), limited to the principal strike-slip zone. As one moves closer to the principal extension zone, the decrease in strike-slip displacement complements the increase in slip vectors. The observed variation is likely attributable to the complexity of the strain field and the interaction between different slip vectors. The variations in the horizontal incremental strain ellipses at each transitional stage indicate the changing trend of the horizontal extension axis (Fig. 18(a) and (b)).

The reactivation of pre-existing faults in the basement results in the oriented arrangement of arcuate splay faults in the cover strata, contributing to the geometric complexity of the fault zone. The splay faults in the caprock remain oblique to the extensional direction, but as the faults continue to grow, the new faults tend to abandon the control of pre-existing discontinuous structures and focus more on the development of planar and continuous major faults. Subsequently, normal faults appear along the most susceptible direction of rupture—perpendicular vertical to the regional stress field. These are key in this process as they facilitate the eventual formation of distinctive large-scale arcuate transtensional faults. Therefore, the linkage process in the intersection area of the transtensional fault system is classified into three stages: isolated-soft linked-hard linked. In the linear strike-slip zone, as the influence of pre-existing structures diminished, the faults no longer exhibit oriented arrangements, thus presenting a progressive evolution model from hard linked to soft linked and ultimately to isolated stage (Fig. 18(b) and (d)). Relay ramps are highly conducive to serve as supply channels for sediment transport. The wide geometry of these relay ramps allows for efficient sediment sorting and accumulation, which is well-documented in previous studies (Harding and Tuminas, 1989; Peacock and Sanderson, 1994; Gawthorpe and Leeder, 2000; Hus et al., 2005). A long and narrow relay ramp is formed at the terminus of each curved transtensional fault, which serves as a promising material source channel. Furthermore, the connection to the normal faults ensures that the relay ramp can directly transfer sediments to deposition centres. The presence of an adequate sediment supply at these depths can provide favourable conditions for oil and gas generation, and the faults that make up relay ramps are highly advantageous for the migration of oil and gas towards shallower layers. Therefore, the

transtensional structure described in this study has great potential for oil and gas exploration.

8. Conclusions

Based on our interpretation of the seismic sections, data statistics, and analogue modelling results, the following conclusions were drawn for the transtensional fault systems in the NPS.

1. Seismic data interpretation and sequential evolution indicate the presence of a sole high dip-angle strike-slip fault during the Eocene. Initially, the pre-existing tectonic morphology exhibited a south-high and north-low characteristic. Since the Miocene, the oblique extension of pre-existing structures has led to the formation of a series of radially arranged splay faults in the overlying strata. Splay faults dip synthetic to reactivated basement faults, collectively forming flower structures. During the ongoing evolution of faults, newly formed fault segments frequently relinquish the control of pre-existing structures and concentrate more on the development of planar and continuous major faults.
2. Arcuate faults can be categorized into linear master fault segments, controlled by pre-existing structures, curved splay faults at termination zones, and young normal faults responsive to regional stress fields. In the case of synchronous fault activity, the intersection zone formed by the two fault systems at the superposition of displacement fields exhibits similar geometric and kinematic characteristics. The curved splay fault in the termination zone, along with the newly formed normal fault, connects to create a long-distance arc-shaped fault.
3. The interaction between faults in the intersection zone was realized through either the hard linkage involving the physical connection of faults or the soft linkage through ductile deformation around faults to transfer displacement. Displacements along the strike were accommodated by linear segments in the principal strike-slip zone, progressive bends of splay faults, dislocations of relay ramps, and dip displacements were accommodated by relay ramps in the overlapping zone. In the principal strike-slip zone, the end of the linear segment was separated toward the movement direction to release the strike-slip displacement in the caprock. Therefore, the transtensional fault system undergoes three stages of isolated-soft linked-hard linked in the intersection zone and a hard linked-soft linked-isolated evolution model in the principal strike-slip zone.
4. The presence of a ductile detachment layer furnishes a crucial material foundation for the efficient transfer of strain. The extensive transmission of strain leads to a more intricate and cohesive interaction among faults. The relationships among faults are significantly strengthened. Without ductile layers, only narrow shear zones and single normal faults would form. Close kinematic processes and geometric forms between different fault systems would not exist. This model aids in comprehending the relationship between different strike faults under the unified stress regime and explaining the genesis of en-échelon faults without PDZ. The intricate inter-fault linkage process in this model also results in the development of relay ramps, proving beneficial for oil and gas exploration.

CRediT authorship contribution statement

Yu-Heng Wang: Writing − original draft, Visualization, Software, Methodology, Investigation, Formal analysis, Data curation. **Fu-Sheng Yu:** Writing − review & editing, Supervision, Resources, Project administration, Investigation, Funding acquisition,

Appendix A. Supplementary data

Supplementary data to this article can be found online at https://doi.org/10.1016/j.petsci.2024.02.017.

References

Allen, M.B., Macdonald, D.I.M., Xun, Z., Vincent, S.J., Brouet-Menzies, C., 1997. Early Cenozoic two-phase extension and late Cenozoic thermal subsidence and inversion of the Bohai Basin, northern China. Mar. Petrol. Geol. 14, 951–972. https://doi.org/10.1016/S0264-8172(97)00027-5.

Arfaoui, A., Soumaya, A., Ayed, N.B., Delvaux, D., Ghanmi, M., Kadri, A., Zargouni, F., 2017. Role of NS strike-slip faulting in structuring of north-eastern Tunisia; geodynamic implications. J. Afr. Earth Sci. 129, 403–416. https://doi.org/10.1016/j.jafrearsci.2017.01.013.

Basile, C., Brun, J.P., 1999. Transtensional faulting patterns ranging from pull-apart basins to transform continental margins: an experimental investigation. J. Struct. Geol. 21, 23–37. https://doi.org/10.1016/S0191-8141(98)00094-7.

Cartwright, J.A., Trudgill, B.D., Mansfield, C.S., 1995. Fault growth by segment linkage: an explanation for scatter in maximum displacement and trace length data from the Canyonlands Grabens of SE Utah. J. Struct. Geol. 17, 1319–1326. https://doi.org/10.1016/0191-8141(95)00033-A.

Chen, X., Li, W., Wu, Z., Yang, H., Zhang, Q., Meng, M., Wang, G., Jia, H., 2022. The tectonic transition from rifting to strike-slip in the Liaodong Bay Depression, offshore China. Mar. Petrol. Geol. 139, 105598. https://doi.org/10.1016/j.marpetgeo.2022.105598.

Cloetingh, S., Van Wees, J.D., Van der Beek, P.A., Spadini, G., 1995. Role of pre-rift rheology in kinematics of extensional basin formation: constraints from thermomechanical models of Mediterranean and intracratonic basins. Mar. Petrol. Geol. 12, 793–807. https://doi.org/10.1016/0264-8172(95)98848-Y.

Cunningham, W.D., Mann, P., 2007. Tectonics of strike-slip restraining and releasing bends. Geological Society, London, Special Publications 290, 1–12. https://doi.org/10.1144/290.10.

Deng, H., McClay, K., 2021. Three-dimensional geometry and growth of a basement-involved fault network developed during multiphase extension, Enderby Terrace, North West Shelf of Australia. GSA Bulletin 133, 2051–2078. https://doi.org/10.1130/B35779.1.

Dooley, T.P., Schreurs, G., 2012. Analogue modelling of intraplate strike-slip tectonics: a review and new experimental results. Tectonophysics 574, 1–71. https://doi.org/10.1016/j.tecto.2012.05.030.

Duclaux, G., Huismans, R.S., May, D.A., 2020. Rotation, narrowing, and preferential reactivation of brittle structures during oblique rifting. Earth Planet Sci. Lett. 531, 115952. https://doi.org/10.1016/j.epsl.2019.115952.

Dunbar, J.A., Sawyer, D.S., 1989. How preexisting weaknesses control the style of continental breakup. J. Geophys. Res. Solid Earth 94, 7278–7292. https://doi.org/10.1029/JB094iB06p07278.

Exadaktylos, G.E., Vardoulakis, I., Stavropoulou, M.C., Tsombos, P., 2003. Analogue and numerical modeling of normal fault patterns produced due to slip along a detachment zone. Tectonophysics 376, 117–134. https://doi.org/10.1016/j.tecto.2003.08.005.

Fodor, L.I., 2007. Segment linkage and the state of stress in transtensional transfer zones: field examples from the Pannonian Basin. Geological Society, London, Special Publications 290, 417–431. https://doi.org/10.1144/SP290.16.

Fossen, H., Rotevatn, A., 2016. Fault linkage and relay structures in extensional settings—a review. Earth Sci. Rev. 154, 14–28. https://doi.org/10.1016/j.earscirev.2015.11.014.

Gabrielsen, R.H., Clausen, J.A., Koyi, H.A., Mancktelow, N.S., 2001. Horses and duplexes in extensional regimes; a scale-modeling contribution. Mem. Geol. Soc. Am. 193, 207–220. https://doi.org/10.1130/0-8137-1193-2.207.

Gawthorpe, R.L., Leeder, M.R., 2000. Tectono-sedimentary evolution of active extensional basins. Basin Res. 12, 195–218. https://doi.org/10.1111/j.1365-2117.2000.00121.x.

Harding, T.P., Tuminas, A.C., 1989. Structural interpretation of hydrocarbon traps sealed by basement normal block faults at stable flank of foredeep basins and at rift basins. AAPG Bull. 73, 812–840. https://doi.org/10.1306/44B4A276-170A-11D7-8645000102C1865D.

Henza, A.A., Withjack, M.O., Schlische, R.W., 2010. Normal-fault development during two phases of non-coaxial extension: an experimental study. J. Struct. Geol. 32, 1656–1667. https://doi.org/10.1016/j.jsg.2009.07.007.

Henza, A.A., Withjack, M.O., Schlische, R.W., 2011. How do the properties of a pre-existing normal-fault population influence fault development during a subsequent phase of extension? J. Struct. Geol. 33, 1312–1324. https://doi.org/10.1016/j.jsg.2011.06.010.

Hu, P., Yang, F., Zhang, R., Wang, W., Dong, R., 2022. Cenozoic extension to strike-slip transition in the Liaodong Bay Subbasin along then-Lu Fault Zone, Bohai Bay Basin: new insights from stress field modelling. Tectonophysics 822, 229163. https://doi.org/10.1016/j.tecto.2021.229163.

Hus, R., Acocella, V., Funiciello, R., De Batist, M., 2005. Sandbox models of relay ramp structure and evolution. J. Struct. Geol. 27, 459–473. https://doi.org/10.1016/j.jsg.2004.09.004.

Kim, Y.S., Sanderson, D.J., 2006. Structural similarity and variety at the tips in a wide range of strike–slip faults: a review. Terra. Nova 18, 330–344. https://doi.org/10.1111/j.1365-3121.2006.00697.x.

Koyi, H., Petersen, K., 1993. Influence of basement faults on the development of salt structures in the Danish Basin. Mar. Petrol. Geol. 10, 82–94. https://doi.org/10.1016/0264-8172(93)90015-K.

Koyi, H., 1997. Analogue modelling: from a qualitative to a quantitative technique—a historical outline. J. Petrol. Geol. 20, 223–238. https://doi.org/10.1111/j.1747-5457.1997.tb00774.x.

Koyi, H.A., Vendeville, B.C., 2003. The effect of décollement dip on geometry and kinematics of model accretionary wedges. J. Struct. Geol. 25, 1445–1450. https://doi.org/10.1016/S0191-8141(02)00202-X.

Li, S., Zhao, G., Dai, L., Zhou, L., Liu, X., Suo, Y., Santosh, M., 2012. Cenozoic faulting of the Bohai Bay Basin and its bearing on the destruction of the eastern north China Craton. J. Asian Earth Sci. 47, 80–93. https://doi.org/10.1016/j.jseaes.2011.06.011.

Liang, Q., Ruoyan, K., Danping, Y., Hongxu, M., Weihua, S., Shouheng, S., Yangguang, H., Chengming, L., Liangliang, Z., Fude, C., Ariser, S., 2022. Paleo-Pacific plate subduction on the eastern Asian margin; insights from the Jurassic foreland system of the overriding plate. Geol. Soc. Am. Bull. 134, 2305–2320. https://doi.org/10.1130/B36118.1.

Liang, J., Yu, F., Liu, G., Tong-kui, W., Ding-hua, L.I., Kui, M.A., 2014. Deformation superimposition characteristics resulting from stretching direction changes in Nanpu Sag: insight from physical modelling. Geoscience 28, 139 (in Chinese).

Liu, M., Cui, X., Liu, F., 2004. Cenozoic rifting and volcanism in eastern China: a mantle dynamic link to the Indo–Asian collision? Tectonophysics 393, 29–42. https://doi.org/10.1016/j.tecto.2004.07.029.

Liu, X., Zhang, C., 2011. Nanpu sag of the Bohai Bay basin: a transtensional fault-termination basin. J. Earth Sci. 22, 755–767. https://doi.org/10.1007/s12583-011-0225-2 (in Chinese).

McClay, K.R., 1990. Extensional fault systems in sedimentary basins: a review of analogue model studies. Mar. Petrol. Geol. 7, 206–233. https://doi.org/10.1016/0264-8172(90)90001-W.

Morley, C.K., Gabdi, S., Seusutthiya, K., 2007. Fault superimposition and linkage resulting from stress changes during rifting: examples from 3D seismic data, Phitsanulok Basin, Thailand. J. Struct. Geol. 29, 646–663. https://doi.org/10.1016/j.jsg.2006.11.005.

Morley, C.K., 2017. The impact of multiple extension events, stress rotation and inherited fabrics on normal fault geometries and evolution in the Cenozoic rift basins of Thailand. Geological Society, London, Special Publications 439, 413–445. https://doi.org/10.1144/SP439.3.

Mouslopoulou, V., Nicol, A., Little, T.A., Walsh, J.J., 2007. Displacement transfer between intersecting regional strike-slip and extensional fault systems. J. Struct. Geol. 29, 100–116. https://doi.org/10.1016/j.jsg.2006.08.002.

Peacock, D.C.P., Sanderson, D.J., 1994. Geometry and development of relay ramps in normal fault systems. AAPG (Am. Assoc. Pet. Geol.) Bull. 78, 147–165. https://doi.org/10.1306/BDFF9046-1718-11D7-8645000102C1865D.

Qi, J., Yang, Q., 2010. Cenozoic structural deformation and dynamic processes of the Bohai Bay basin province, China. Mar. Petrol. Geol. 27, 757–771. https://doi.org/10.1016/j.marpetgeo.2009.08.012.

Ramberg, H., 1981. Gravity, deformation, and the earth's crust. In: Theory, Experiments, and Geological Application. Academic Press.

Rojo, L.A., Koyi, H., Cardozo, N., Escalona, A., 2020. Salt tectonics in salt-bearing rift basins: progradational loading vs. extension. J. Struct. Geol. 141, 104193. https://doi.org/10.1016/j.jsg.2020.104193.

Schellart, W.P., Lister, G.S., 2005. The role of the East Asian active margin in widespread extensional and strike-slip deformation in East Asia. J. Geol. Soc. 162, 959–972. https://doi.org/10.1144/0016-764904-112.

Soliva, R., Benedicto, A., 2004. A linkage criterion for segmented normal faults. J. Struct. Geol. 26, 2251–2267. https://doi.org/10.1016/j.jsg.2004.06.008.

Tong, H., Zhao, B., Cao, Z., Liu, G., Dun, X.M., Zhao, D., 2013. Structural analysis of

faulting system origin in the Nanpu sag, Bohai Bay Basin. Acta Geol. Sin. 87, 1647–1661. doi:10.19762/j.cnki.dizhixuebao.2013.11.002. (in Chinese).

Weijermars, R., Schmeling, H., 1986. Scaling of Newtonian and non-Newtonian fluid dynamics without inertia for quantitative modelling of rock flow due to gravity (including the concept of rheological similarity). Phys. Earth Planet. In. 43, 316–330. https://doi.org/10.1016/0031-9201(86)90021-X.

Wilson, P., Hodgetts, D., Rarity, F., Gawthorpe, R.L., Sharp, I.R., 2009. Structural geology and 4D evolution of a half-graben: new digital outcrop modelling techniques applied to the Nukhul half-graben, Suez rift, Egypt. J. Struct. Geol. 31, 328–345. https://doi.org/10.1016/j.jsg.2008.11.013.

Woodcock, N.H., Fischer, M., 1986. Strike-slip duplexes. J. Struct. Geol. https://doi.org/10.1016/0191-8141(86)90021-0.

Wyrick, D.Y., Morris, A.P., Ferrill, D.A., 2011. Normal fault growth in analog models and on Mars. Icarus 212, 559–567. https://doi.org/10.1016/j.icarus.2011.01.011.

Xu, H., Wang, X.-W., Yan, D.-P., Qiu, L., 2018. Subsidence transition during the post-rift stage of the Dongpu Sag, Bohai Bay Basin, NE China: a new geodynamic model. J. Asian Earth Sci. 158, 186–199. https://doi.org/10.1016/j.jseaes.2018.03.001.

Yu, F., Koyi, H., 2016. Cenozoic tectonic model of the Bohai Bay Basin in China. Geol. Mag. 153, 866–886. https://doi.org/10.1017/S0016756816000492.

Zhao, R., Chen, S., Wang, H., Gan, H., Wang, G., Ma, Q., 2019. Intense faulting and downwarping of Nanpu sag in the Bohai Bay Basin, eastern China: response to the Cenozoic stagnant Pacific slab. Mar. Petrol. Geol. 109, 819–838. https://doi.org/10.1016/j.marpetgeo.2019.06.034.

Zhu, Y., Liu, S., Zhang, B., Gurnis, M., Ma, P., 2021. Reconstruction of the Cenozoic deformation of the Bohai Bay Basin, north China. Basin Res. 33, 364–381. https://doi.org/10.1111/bre.12470.

Zwaan, F., Schreurs, G., Rosenau, M., 2020. Rift propagation in rotational versus orthogonal extension: insights from 4D analogue models. J. Struct. Geol. 135, 103946. https://doi.org/10.1016/j.jsg.2019.103946.